The thesis committee for Spencer Windhorst Jolly certifies that this is the approved version of the following thesis

Two-Color High Intensity Laser Plasma Interaction Phenomena, and Status of Experiments on the UT^3 Laser System

APPROVED BY

SUPERVISING COMMITTEE:

Michael C. Downer, Supervisor

Gennady Shvets

Two-Color High Intensity Laser Plasma Interaction Phenomena, and Status of Experiments on the UT^3 Laser System

by

Spencer Windhorst Jolly, B.S.E.

THESIS

Presented to the Faculty of the Graduate School of
The University of Texas at Austin
in Partial Fulfillment
of the Requirements
for the Degree of

MASTER OF ARTS

THE UNIVERSITY OF TEXAS AT AUSTIN
May 2014

For my parents

Acknowledgments

I would like to thank those close to me for support, both emotional and tangible. This includes most notedly my parents Robert and Lorraine, without whom I would not be the man I am today. And my better half Irena Pereša. Although she is the reason I am leaving Texas early, she played a big part in my late term successes and motivation on this work, along with my sanity during some hard times.

I would like to thank J.C. Sanders, who was the workhorse of this work and the main contributor to many daily tasks during laser runs. Although my role was to assist him it is crucial to note that without his consistent work we would not be near as far on these two-color experiments as we are today.

Additionally, productive talks with Rafal Zgadzaj, Xaioming Wang, and others were crucial at certain points of the last two years, and during crisis points during laser runs. I thank them for their expertise and input.

Lastly, I thank Mike Downer for providing me with the opportunity to do the work that I have at the University of Texas and to gain the skills I have while working on the UT^3 system. If it were not for him and this lab I would not have grown over these two years as I have. I leave the University with a much more vast and important skill set than when I entered, which will stay with me forever. For this I am very thankful.

Two-Color High Intensity Laser Plasma Interaction Phenomena, and Status of Experiments on the UT^3 Laser System

Spencer Windhorst Jolly, M.A.
The University of Texas at Austin, 2014

Supervisor: Michael C. Downer

We report the status of two-color high intensity laser-plasma interaction experiments on the UT^3 laser system at the University of Texas at Austin. After an outline of the experimental apparatus, an overview of the motivating theoretical work, and a characterization of the performance of our Chirped Pulse Raman Amplification system (CPRA) we report the status of our most recent experiment. We have attempted to seed the growth of the Raman Forward Scattering (RFS) instability in order to produce electrons at lower driving pulse power than is conventionally needed. We have been unsuccessful, and provide reasons why and recommendations for future modifications to the experimental apparatus. The most significant conclusion is that the CPRA system as it is now is not appropriate for this experiment because the observed RFS spectrum is at higher wavelength than our system. Possible future changes include either amplifying a separate barium nitrate sideband at 938 nm through the CPRA system or using a different Raman active medium after the main 800 nm UT^3 pulse is compressed. The feasibility study of these possible modifications is not yet complete.

Table of Contents

List of Tables

List of Figures

Chapter 1

Introduction

1.1 Scientific Motivation

Laser wakefield acceleration (LWFA) is a phenomenon that had been predicted for a significant amount of time [1], but relies on high intensity lasers that have only been in existence for a few decades since the development of Chirped Pulse Amplification (CPA) [2]. As laser technology has developed so has the understanding and performance of this phenomenon. Recent advances on the Petawatt laser here at the University of Texas at Austin [3] in addition to projects throughout the U.S. and the world have pushed the boundaries of the energy of accelerated electrons in addition to the quality of secondary light sources produced therein.

Here in Michael Downer's Terawatt lab we have a maximally 45 TW Titanium Sapphire based laser system that is in place to significantly explore and optimize laser-plasma processes that are related to LWFA. This laser system (Chapter 2) is a combination of a Femtopower [4] and Thales industrial laser infrastructure and target chamber optics and diagnostics made in house. It operates at 800 nm, can be compressed to almost 30 fs, and reaches relativistic intensities. F. Grigsby [5, 6] and J.C. Sanders [7] have made and fine-tuned respectively a system that Raman shifts a small fraction of the main laser pulse to 873 nm, amplifies it to above 100 mJ, and compresses to nominally 200 fs. It is this two-color setup that is used for the experiment done in this thesis.

A set of four main motivating theoretical phenomenon (Chapter 3) are outlined: The seeding of Raman Forward Scattering [8] (RFS) in order to produce accelerated electrons in the self-modulated regime at lower driving pulse powers than usual, a scenario to mitigate the relativistic self-focusing mechanism [9, 10], a schematic to enhance acceleration and injection LWFA experiments using counter-propagating beams of different colors [11], and a technique to use plasma effects to turn two compressed beam of different color to create a train of few fs pulses [12]. These phenomenon motivate the existence of the CPRA system and our work.

The experiment that has been first attempted so far is the first listed. We have attempted to seed RFS in order to observe enhancement of the plasma wave and acceleration of electrons at driving pulse powers below the critical power for self-focusing (Chapter 5). However, we have so far been unsuccessful. A number of issues are discussed in addition to possible solutions and action points moving forward.

1.2 Practical Matters

For most of this work primary sources are used. By that I mean that papers either showing a theory or an experimental result are cited properly and directly. However, for some sections secondary sources such as review papers or textbooks are used. This especially includes Robert Boyd's nonlinear optics text book [13], William Kruer's text on Laser Plasma Interaction [14], and Eric Esarey's 2009 review of laser-based electron accelerator physics [15]. It is crucial to include these works because of their usefulness, but also because they are exceptional sources for further publications. I make an attempt to cite specific primary resources when appropriate, but I must note that these listed works do a more comprehensive job. I implore the reader to consult these among others for very instructive content, but also for extremely thorough citations.

Additionally, SI units are used everywhere unless very obviously noted. The electron charge is always $-e$, meaning that the constant e is positive.

Often there are references to the a_0 parameter, the "normalized vector potential". This is a normalized parameter that reflects the strength of the laser pulse and is a reflection of the ability of the pulse to oscillate electrons in a plasma such that they are relativistic. Specifically, $a_0 = eA/mc$, or as an engineering formula, $a_0^2 = 7 * 10^{-19} \lambda^2 [\mu m] I [W/cm^2]$, where λ is the laser wavelength and I is the intensity in familiar units. As a_0 approaches 1 the electrons have a significantly relativistic quiver momentum and therefore a relativistic mass increase when under the influence of the laser field.

Chapter 2

Experimental Apparatus

This chapter will explain the details of the UT^3 laser system, albeit in only a concise manner. Also, a novel diagnostic tool for viewing two separate spectra from the interaction chamber will be detailed.

2.1 UT^3 Main System

The UT^3 laser system is a laser built mostly by industrial sources (FEMTOPOWER and THALES), which operates at 800 nm via Titanium doped Sapphire amplifier crystal. It is pumped at different stages by diodes, Nd:YLF, and Nd:YAG green lasers to pump the prominent absorption for Ti:Sapph in that range. It's peak energy after all stages has been shown to be ∼1.3 J. That pulse compressed to ∼30 fs and focused to ∼10 μm can achieve relativistic intensities. This section will provide a concise outline of the various subsystems of the laser.

The first major component of the laser system is the FEMTOPOWER Compact Pro short pulse system (diagram in Fig. 2.1 and flow chart in Fig. 2.2. This is an industrial system which is often used by scientific labs for short pulse work that does not require higher energies or contrast. Of course in our lab we use it to create the initial pulse which be amplified afterwards.

The laser starts with an Nd:vanadate laser pumping a small Ti:Sapph crystal, which is mode-locked and operates at 76 MHz. This is a resonator cavity [16] that is mode-locked using the passive Kerr lens technique. Mirrors within the cavity provide a chirp to the pulse. The pulse, after output, is stretched using a simple glass stretcher. Then the pulse is sent through the first four passes of what we call the "9-pass" amplifier, which is the first free space amplifier in the chain.

The 9-pass amplifier is pumped by 8 W from a 20 W, 1 KHz Nd:YLF laser known as the "JADE". This laser pumps the amplifier in two passes via retro-reflection. The seed pulse makes four passes still at 76 MHz and then goes through a high-voltage powered 1 KHz Pockels Cell (Pulse Selector) and proceeds to make 5 more passes. The pulse is then compressed in a set of prisms and exits the FEMTOPOWER Compact Pro System.

In order to do many laser-plasma experiments high contrast is required. Because of this, the compressed pulse is then sent through an XPW system (Cross-Polarized Wave generation) in order to increase the contrast. Energy is lost, but it in the interest of contrast, which is absolutely necessary. After this the pulse is then once again stretched and finally ready to be amplified to its maximum.

First a "Booster" amplifier recovers the energy lost through the XPW while the pulse is still at a 1 KHz repetition rate. The Booster is pumped by the remaining energy from the 20 W JADE. Then a high-voltage 10 Hz Pockels Cell (Pulse Cleaner) selects pulses for the final, high energy stages (Fig. 2.3). These last two stages, the "Pre-Amp" and "Power-Amp" are together pumped by up to four, but usually three Nd:YAG, 10 Hz lasers. After this the pulse is finally sent through the compressor system and in to the interaction chamber. Everything after the amplifiers is in vacuum to avoid damage and degradation

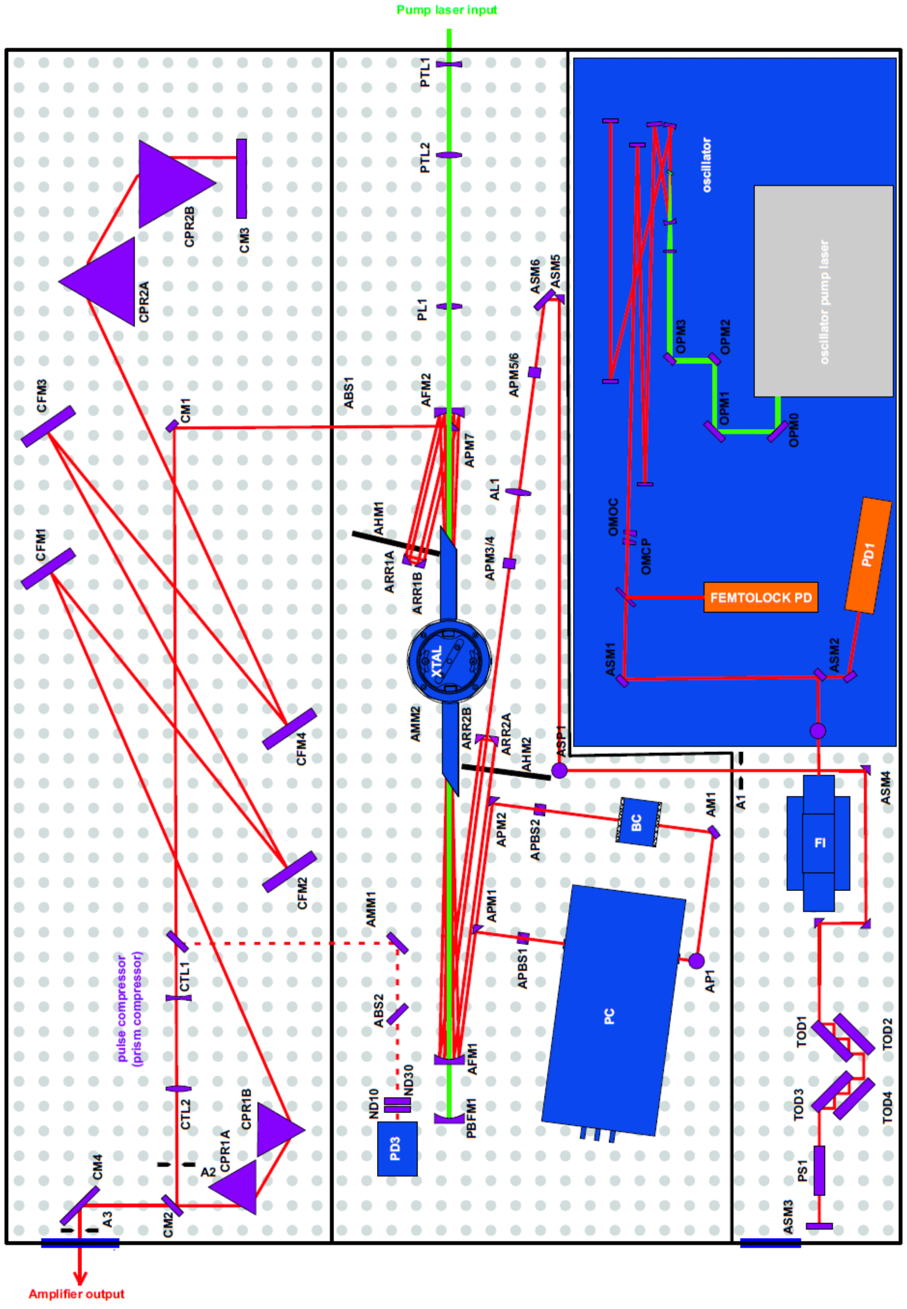

Figure 2.1: Detailed optical diagram of the FEMTOPOWER Compact Pro [4]. See text for more detailed discussion.

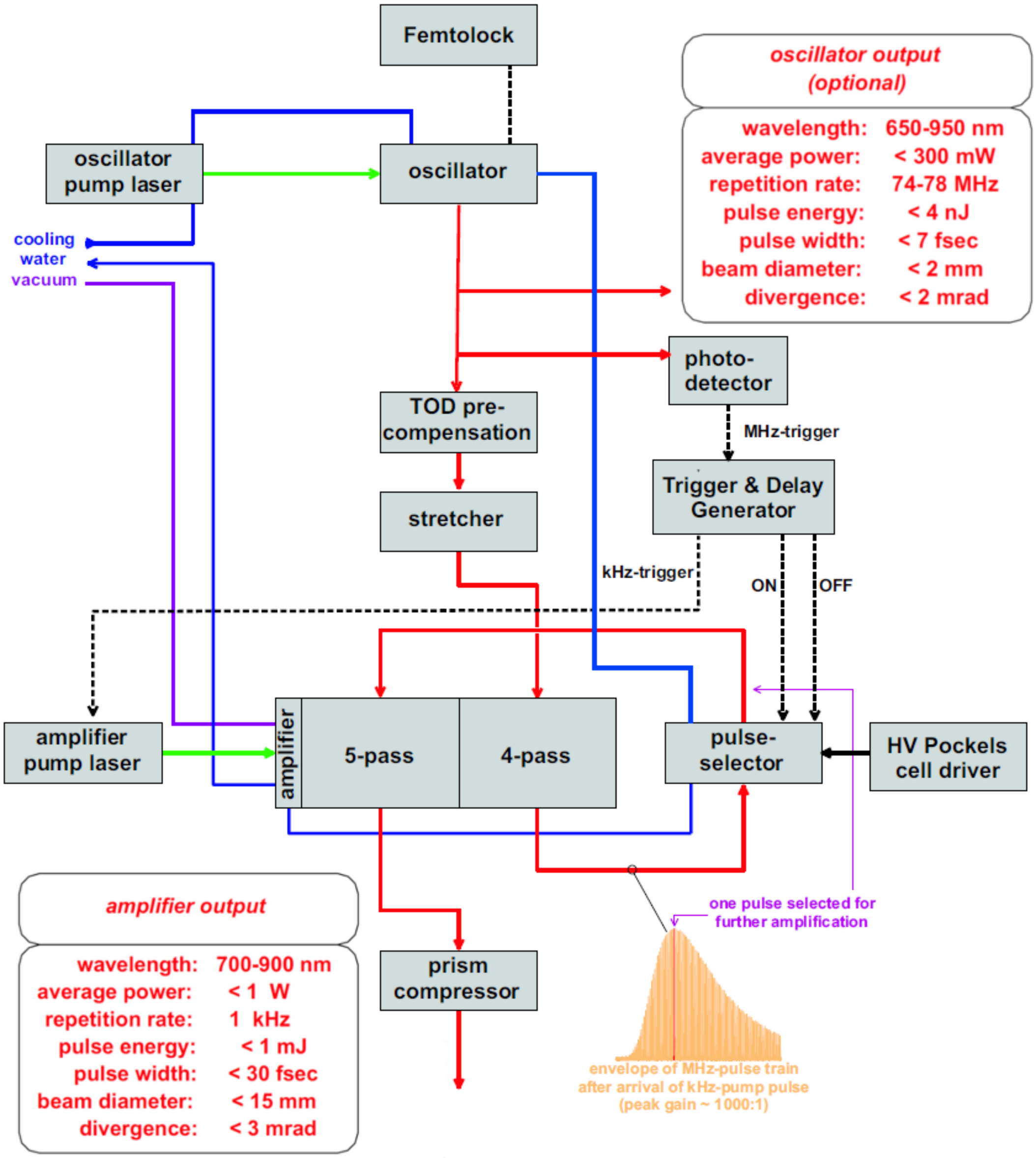

Figure 2.2: Organization chart of the FEMTOPOWER Compact Pro [4]. See text for more detailed discussion.

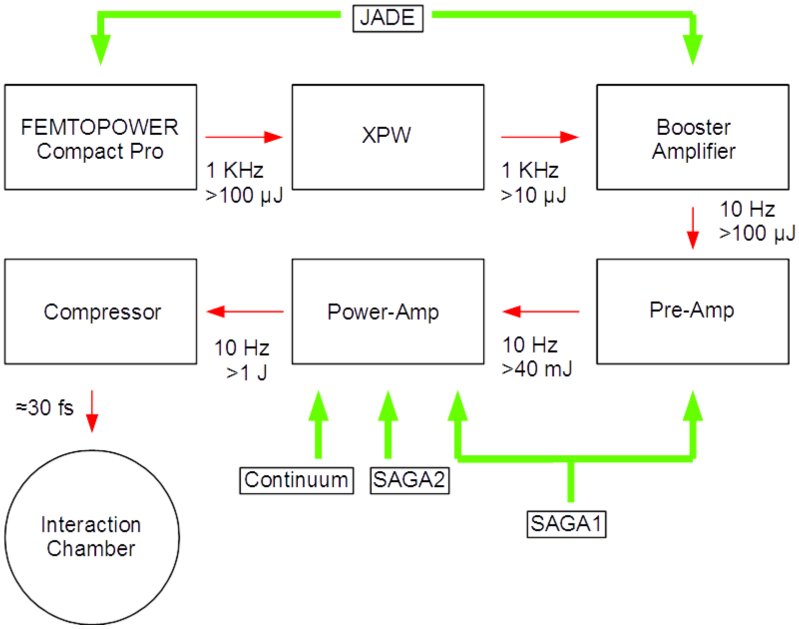

Figure 2.3: Diagram of the stages of the UT^3 laser system with approximate pulse Energies. Note that pulse is stretched after the XPW in order to be amplified further.

of the optics.

2.2 Chirped Pulse Raman Amplification System

The hallmark system that provides the unique second color in order to perform two-color laser-plasma experiments is the Chirped Pulse Raman Amplification System (CPRA). This system splits off some energy from the main driving pulse (after amplification) and Raman shifts it in a Ba$(NO_3)_2$ crystal to create 873 nm light. This light is still chirped and stretched, is amplified through one Titanium Sapphire stage, and then compressed just as the main beam is. This Raman beam is then combined with the main beam path through a special dicroic mirror and is focused using the same off-axis parabola (OAP).

After the final amplification of the 800 nm pulses the beam is split 90/10 in order to have 90% of the energy continue on to be compressed and drive interactions and 10% to be used for the transverse probe (or other experiments) and for the generation of the Raman sideband. This 10% is further split so that only half of the energy goes into the probe line and half goes to the CPRA system.

The CPRA system consists of three stages of amplification. The first stage includes two Ba$(NO_3)_2$ crystals on a long linear stage. The low energy 800 nm beam is focused through these crystals and the crystals are moved along the path to optimize spectrum and energy [7]. This stage is unseeded and is where the 873 nm light is created. The second stage is a seeded stage again through a Ba$(NO_3)_2$ crystal in a non-colinear geometry for optimum phase matching. The exact beam path of these first two stages is shown in

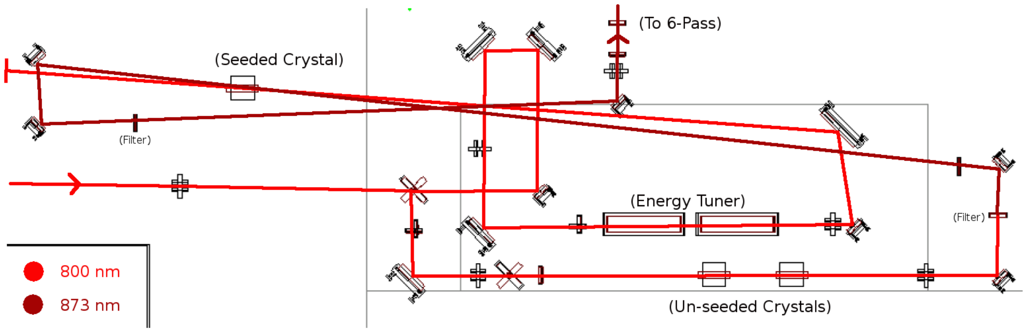

Figure 2.4: Detailed optical diagram of the CPRA system showing the path through the first two amplification stages. The third stage is a simple 6-pass bow-tie geometry through a Ti:Sapph crystal.

Figure 2.4 with a slight variation in color in order to differentiate between the incident 800 nm light and the produced and amplified 873 nm light.

After these first two stages the incident 800 nm light is dumped and any higher order sidebands are filtered out. This leaves only the 873 nm beam, which is still stretched and chirped, and at this point on the order of 1 mJ. This beam then enters a conventional 6-pass Titanium Sapphire amplifier in a bow-tie geometry. This third stage is pumped with a 1 J Quanta Ray laser operating at 532 nm in a bi-directional configuration. At the end of the stage the beam has been as high as 300 mJ on occasion, but operates fairly consistently with an average above 100 mJ.

The Raman beam is then compressed using a two-grating configuration to durations below 200 fs and combined with the main beam path using a dicroic mirror with high reflection at 800 nm and high transmission (from the back face) at 873 nm. From then on the Raman beam is aligned with the main beam and focused on target.

In order for the main beam and the Raman beam to be overlapped in

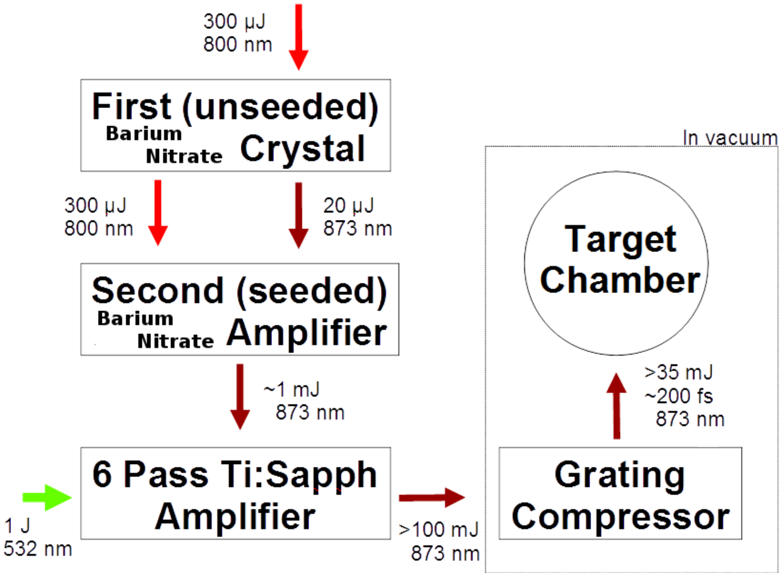

Figure 2.5: Conceptual chart showing the evolution of the Raman system as the beam is produced and further amplified. Many of these numbers change frequently as optimum conditions are not constant. The numbers listed are only a guide. The performance of the six pass amplifier varies from time to time along with the efficiency through the gratings.

time, which is required of most experiments, there is a very long (20 m) delay line for both the full energy main beam and the transverse probe diagnostic beam. This delay line is to compensate for the significantly longer path of the beam through the CPRA system. As will be described in a later section, rough time overlap has been routinely achieved.

2.2.1 A Comment on Stability

Figure 2.5 shows a flow-chart based evolution of the Raman pulse through the CPRA system. it is very important to note that, although these numbers are a fair representation of the system, they are not necessarily typical or very precise [7]. For example, we have seen in the past energies upwards of 300 mJ out of the final stage, but have much more typically seen average energies slightly above 100 mJ. Additionally, we have seen durations lower than 100 fs after the compressor, but more typically see average durations of about 200 fs. We often have to iris the beam in order to increase the mode quality, which then decreases energy that continues on through the amplifier stages. Because the size of the aperture needed to achieve a beam of adequate quality is not consistent we can lose energy consistency even if it existed initially.

Although it is possible in one instance to characterize these distributions, neither in one instance or over any long period of time have the conditions necessary for a given performance or the exact distribution of that performance been consistent. For some period energy may be consistent, but spectrum is more narrow leading to worse compression. For some other time period spectrum may be acceptable, but some or all of the amplifier stages are operating poorly. And what is more typical is that all parameters are operating at an OK level, leading to all parameters being less than ideal, which results is much lower than ideal on-target intensity.

Although this thesis will not detail these stability problems any more, a more thorough approach can be found in J.C. Sanders's PhD Dissertation [7]. The instabiliy of this system, and the fact that it has not been traced to any reliable source except for the instability of the whole laser system itself, has been the most significant damper to progress on the experiments (as detailed later).

2.3 Interaction Chamber

Although the laser system (especially including the CPRA system) is suitably complex, the real experiments are done in the vacuum chamber re-

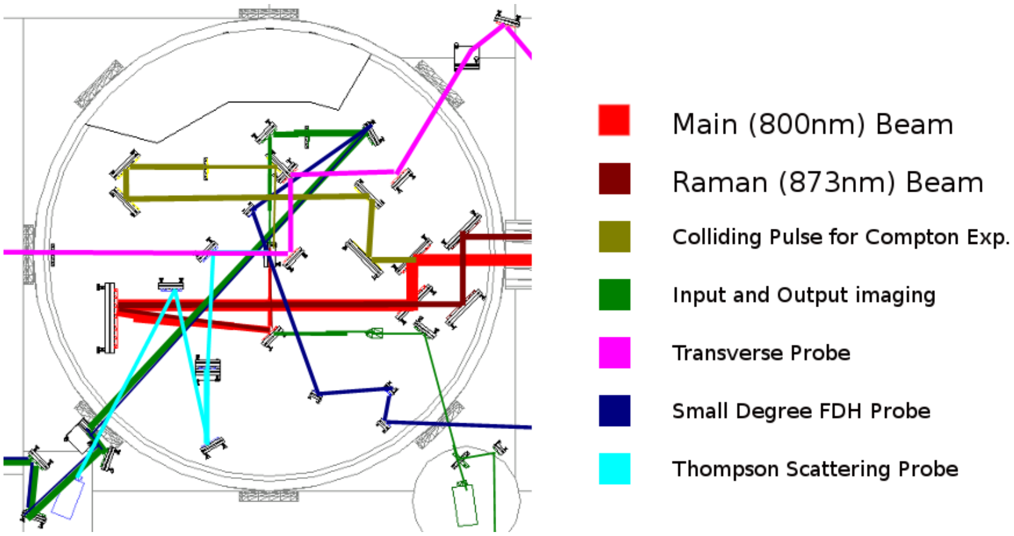

Figure 2.6: Detailed layout of the wakefield chamber use as of 2013. Beams are in color on the digital copy. Courtesy of J.C. Sanders.

ferred to as the ”wakefield chamber” or the ”interaction chamber”.

This chamber is full of optics and contains a full suite of diagnostics. A diagram, which is most easily discernible in color as seen in Fig. 2.6 includes every possible optical path and most diagnostics. These diagnostics include an imaged top-view Thompson scattering system, a transverse probe for interferometry (Fig. 2.8), a small-degree frequency domain holography (FDH) probe at 400 nm, and imaging systems for both the input focal spot and the output spatial mode. It goes without saying that not all of these diagnostics are generally used at one time.

Although the diagnostics are important, the centerpiece of the interaction chamber is the final delivery of the high energy compressed beams. These beams are focused using an off-axis parabolic mirror (OAP) and directed to be in focus directly over a gas jet nozzle (at the center of the chamber). This

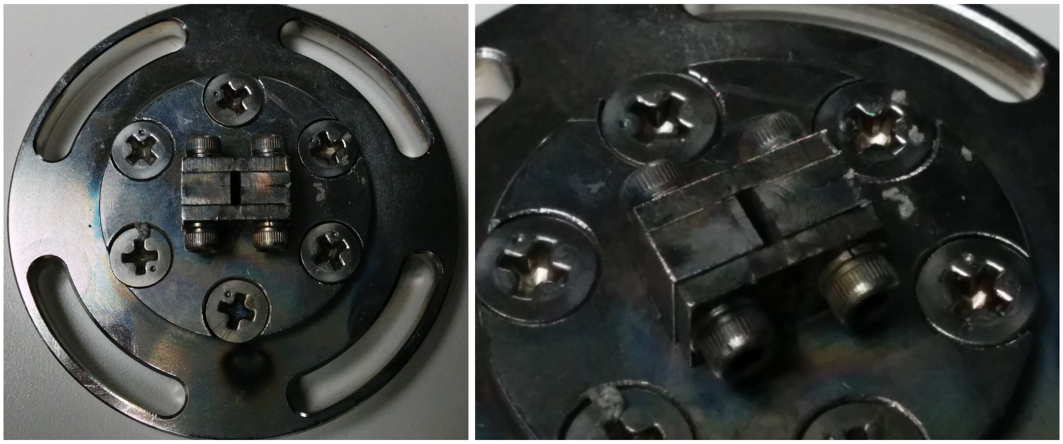

Figure 2.7: Top view (left) and zoomed-in view (right) of the gas jet nozzle used in wakefield and other plasma experiments.

gas jet nozzle (SmartShell Co., Ltd.) delivers a puff of gas at variable pressure for interaction with the high-intensity laser light. The nozzle can be see in Fig. 2.7. It has two possible lengths, 1 mm and 3 mm. It is specially designed to operate in the supersonic regime [17, 18] and have a 200 μm rising edge in gas density. It is on a three axis, motor controlled stage that allows for exact control of where the focus is in relation to the entrance of the gas plume.

The laser light immediately ionizes the gas and can produce accelerated particles through laser wakefield acceleration (Appendix A). Additional diagnostics for this process include a magnet for deflecting the electrons and thus measuring the energy, and a multi-channel plate for X-ray measurements. A sample (rough) interferogram can be seen in Fig. 2.8 along with electrons optimized by H.-E. Tsai [19].

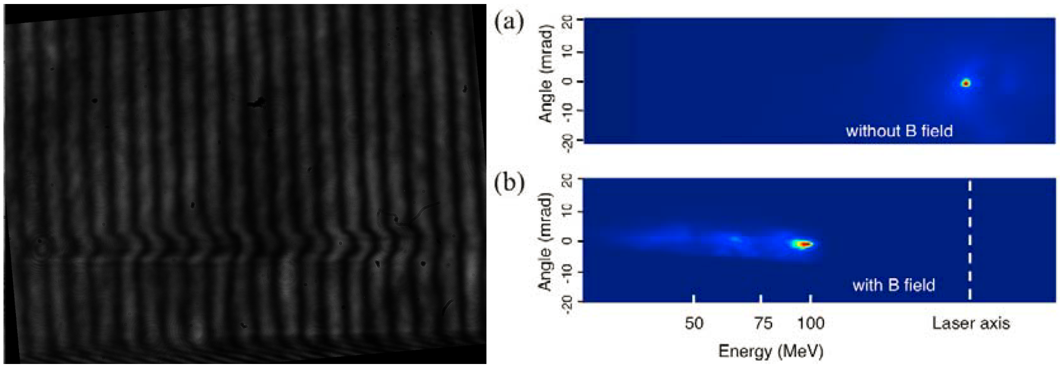

Figure 2.8: Raw interferogram (left) of the main 800 nm beam focused ∼500 μm above the gas jet and an example of electron spectrum (right) produced from a separate, more optimized interaction. The electron data shows low divergence (a) along the laser axis with no deflecting B-field and low energy spread (b) with deflection [19].

2.4 Grating Spectrometer Diagnostic Tool

One of the most significant practical hurdles for diagnostics in the interaction chamber is that there is not much space available. This is both physical space inside and adjacent to the chamber, but also space for optical paths. One of the first possible test experiments for the Raman system, the measurement of relativistic cross-phase modulation (Sec. 4.2.2) requires the measurement of the output spectrum. Additionally because the Raman beam experiences significant fluctuations, the measurement of the input spectrum is also desired. There was simply no space in the current setup to allow for either of those diagnostics.

Therefore, I designed a simple attachment (Fig. 2.9) to allow for both the input and output spectrum to be measured at once on the CCD of a large grating spectrometer located across the lab. Because of the long distance, a 10 m fiber was used to transport the light across the lab. The attachment

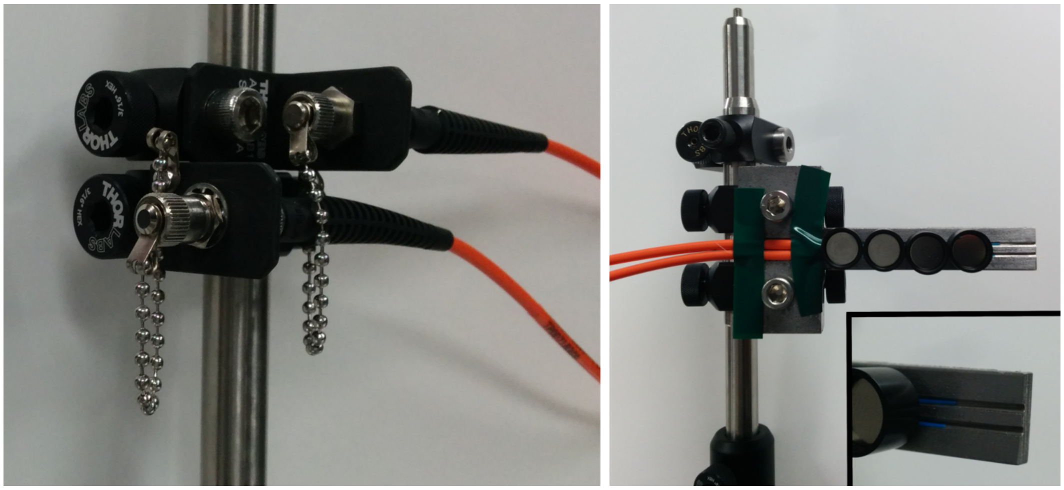

Figure 2.9: Close up of the SMA threaded inputs (left) and the custom machined fiber output (right) with a closer view of the grooves for the bare fibers (inset).

collected the light from the transport fiber(s) and eventually was coupled in free space in the input slit for the grating spectrometer.

Although we decided to use a simple commercial fiber spectrometer to measure the output spectrum (due to the high bandwidth needed), this diagnostic tool was still useful in measuring the input spectrum for the Raman beam. It was easy to show that two signals can be read at once, and that both incident spectrum can be read in one of the inputs (Fig. 2.10)

The input spectrum is taken from the input imaging line shown in Fig. 2.6 via a simple beam-splitter and transported via the 10 m fiber across the lab. Output spectrum is similarly split from the output imaging system.

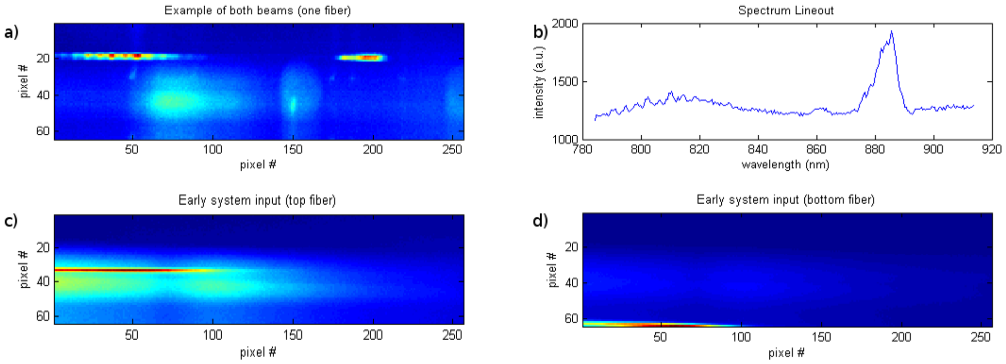

Figure 2.10: Raw CCD image (a) of both amplified main beam and Raman beam on the input spectrometer with spectrum lineout (b). (c) and (d) are examples of early system 800 nm light on both the top and bottom input fiber respectively. Note that the background is not subtracted.

Chapter 3

Theoretical Motivation

This section is a summary and experimental description of the scenarios described in a number of theoretical and experimental papers [8, 9, 11, 12, 20, 21]. It must not be downplayed that these papers are a significant influence and a serious motivation for the experiments on the CPRA system.

This section will provide a brief explanation of multiple motivating phenomena for two-beam, two-color laser-plasma experiments. Hopefully the viewpoint of an experimentalist will add unique substance to these sections.

3.1 Raman Seeded Wakefield Acceleration

This section is a summary of [8], which is the main experiment first attempted on the CPRA system. See Chapter 5 for a detail of our progress on the experiment.

Wakefield acceleration in general requires very high intensity laser pulses ($> 10^{18} W/cm^2$) to create a large enough wake to excite an accelerating structure and trap electrons. In the self-modulation regime the envelope of the pulse is modified by the Raman forward scattering (RFS) instability, and electrons with a continuous energy spectrum up to the high MeV level can be produced. This result has been shown experimentally almost two decades ago [22].

Although laser technology has been enhanced, the types of lasers that

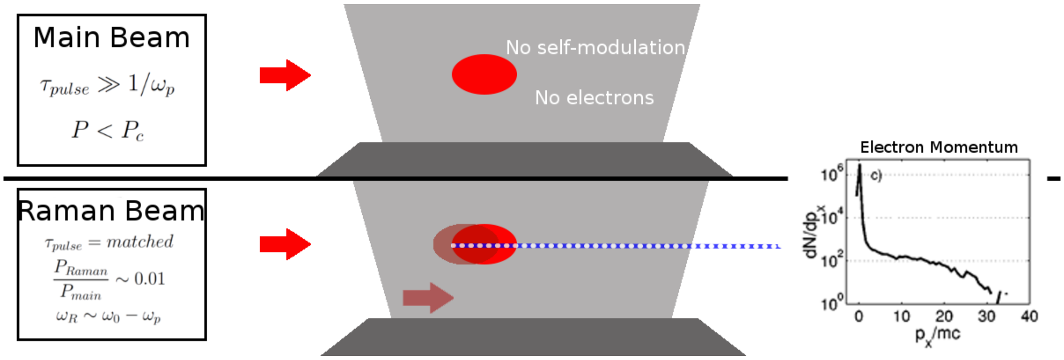

Figure 3.1: Cartoon showing the essence of the Raman seeding experiment. The intense driving pulse should not be intense enough to produce electrons by itself (top), but with the Raman seed co-propagating there should be continuous electrons with energies of up to 10s of MeV (bottom) [8].

can produce this regime are still considered high-intensity lasers and are not generally operated at rep-rates larger than 10 Hz, and effectively many are below that rate. However, it is desirable to have electrons like these available to do experiments at a high rep-rate up to or above 1 kHz.

Because the self-modulated LFWA regime is achieved due to the growth of the forward Raman instability within the plasma it is thought that seeding of the forward Raman instability will lower the driving laser intensity threshold down to the level where kHz rep-rates are achievable. A detailed computational study showing that this is the case was done in 2005 [8]. Of course this requires experimental verification.

The scenario described is that a much lower intensity beam (1%) detuned in frequency by approximately the plasma frequency is aligned to be collinear within the plasma. If temporal overlap is achieved then it is possible to seed the forward Raman instability and therefore seed the growth of the wakefield. It is this wakefield that will produce accelerated electrons, but at a much lower driving pulse intensity ($a_0 = 0.5$ for example) than would otherwise be needed ($a_0 > 1$).

In order to achieve this scenario (Fig. 3.1), we must have pulses of two colors compressed to approximately the same duration. The driving beam must be sub-critical in order to not experience self-focusing and therefore not have the envelope modulated due to that instantaneous increase in intensity. This beam, and therefore both beams must also be well above the matched wakefield condition ($k_p L_{RMS} = 1$, Appendix **??**), so that the Raman instability can grow once seeded (see Appendix B.3).

The hope is that with the driving beam alone there will be no electrons. The initial conditions are such that this will surely be the case. When the Raman beam is also incident on the plasma and adequately overlapped with the driving beam then electrons will be produced. The small inset in Figure 3.1 shows an example of the electron spectrum expected for similar conditions to those described.

This experiment is the main experiment attempted on our own CPRA system, with the progress so far detailed in Chapter 5.

3.2 Control of Relativistic Self-Focusing

This section is a summary of the scenario proposed in [9, 10].

Relativistic self-focusing (RSF, see Appendix C), is a phenomenon that occurs often in laser-plasma interaction experiments. Because of this it is desirable to suppress relativistic self-focusing in certain scenarios, and enhance it on others. In general if the effect of self-focusing can be controlled rather than being an instability, it is advantageous in a wide range of applications. It has

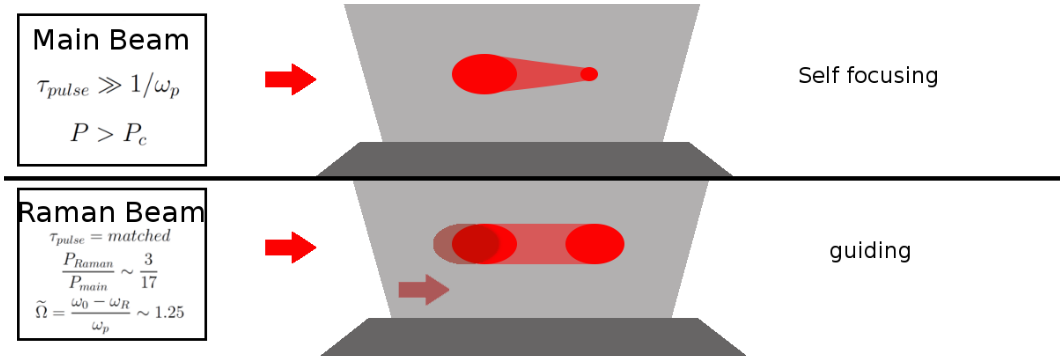

Figure 3.2: Graphical depiction of the RSF suppression experiment. The over-critical main beam should focus within the plasma (top), but when the lower energy detuned beam is present the main beam will not experience self-focusing (bottom). If the tuning is such that the difference in frequency is less than the plasma frequency, RSF can be enhanced and the effect would be the opposite as pictured.

been shown through a computational study that a co-propagating pulse detuned by just over the plasma frequency can suppress relativistic self-focusing of a driving beam, and enhance it when detuned by less than the plasma frequency [9, 10].

This mechanism is caused by the electron density perturbation from the low amplitude beatwave. This 3D perturbation, when the detuning is greater than the plasma frequency, provides a defocusing mechanism that over-balances RSF and can achieve guiding in an situation that would otherwise be over-critical.

The first study provides a brief analytic explanation, but the bulk of the results are taken from WAKE simulations, a 3D Particle-in-cell (PIC) code. The specific scenario [9] is an overcritical monochromatic pulse experiences RSF and collapses in less than two Rayleigh lengths when the pulse is by itself. When a lightly detuned pulse ($\omega_0 - \omega_R = 1.25\omega_p$) is co-propagating, the overcritical driving pulse no longer collapses and is guided for over three Rayleigh lengths. When a strongly detuned pulse ($\omega_0 - \omega_R = 3.18\omega_p$) is present, RSF is no longer mitigated. The power partition between the driving pulse and detuned pulse is 17/3.

A complementary scenario is observed in [10], where the second color beam is under-detuned and results in enhancement of self-focusing. Specifically the detuning is $\omega_0 - \omega_R = 0.9\omega_p$, and the power is now equally partitioned between the two beams (2.25 TW in each beam). The author notes that in this case the dynamics are heavily dependent on the initial laser pulse shape and pulse duration. This is a significant note in the context of the Petawatt experiments.

The pulse lengths in these examples are all well above the pulse durations that are normal for the UT^3 system, but with the proper choice of parameters I believe that this experiment is within the capabilities of the system. In fact, J.C. Sanders has prepared infrastructure to create pulses of the appropriate spot size, and they are mostly ready to be added to the interaction chamber.

3.3 Colliding Beam Accelerator

This section is a summary of the scenario proposed in [11, 20] along with related experimental results from [21].

In [21] a study is done involving two counter-propagating beams. One beam has an intensity of $a_0 = 1.3$, which drives the wakefield and produces accelerated electrons. The second beam, which is collinear and counter-propagating has an intensity of $a_0 = 0.4$ and is used to force injection of electrons in to the wake of the driving pulse. By decreasing the plasma density to below the self-injection threshold (with only the driving beam), the production of accelerated electrons was eliminated. Then, the injection pulse was sent in with the driving pulse and the production of electrons was recovered by virtue of the forced injection due to the second pulse. A detailed time-delay study was done showing the dependence of the maximum electron energy and δE/E as a function of injection position within the gas jet (see inset in Fig. 3.3).

This result is significant because it characterizes the dependence of parameters on the location of injection in addition to proving the viability of a counter-propagating geometry. It must be noted of course that these beams are both the same color and that the injection of electrons is ostensibly a product of the "beatwave" produced between different frequency components of these broadband pulses. Previous theoretical work [11, 20] proposes a counter-propagating scenario involving up to three beams and up to three colors ()thereby producing a beatwave from the different center frequencies).

The first theoretical study [20] outlines the acceleration of electrons using three pulses similar to Fig. 3.3 of three different colors and in general up to two different pulse durations. However, these simulations are done at significantly lower densities (less than $10^{18} cm^{-3}$) than most short pulse LWFA experiments in this field today, albeit closer to the densities relevant to the recent experiments on the Texas Petawatt (see A). However, the pulse durations referenced are significantly longer than both short pulse systems and the Texas Petawatt. The dynamics are more related to a traditional beatwave accelerator with a counter-propagating beam used to increase the accelerating field amplitude. Despite that, This paper is a significant study of the growth of plasma waves caused by detuned and counter-propagating pulses.

A more recent study in [11] outlines multiple scenarios that involve at least one driving beam and one counter-propagating beam. The first two proposals are in the paper itself said to be difficult to achieve experimentally.

The first scenario, referred to as the ”super beatwave” is similar to what was described in [20]. Three beams, three colors, and one of the beams counter-propagating to ”pump” the beatwave and increase the accelerating gradient. With all three pulses at a similar duration, $\omega_p \tau_L = 25$, the pump beam can enhance the accelerating gradient up to more than 12 GeV/m. However, as is noted in the paper (and echoed by this author), three intense beams is a very difficult experimental scenario let alone three beams all of different colors.

The second scenario is referred to as a more conventional colliding beam accelerator (CBA). There are now only two beams, but the driving beam is very short, $\omega_p \tau_L = 2.0$. There is a threshold intensity where the counter=propagating beam will lead to a larger accelerating gradient, which is a very achievable level. However, as the paper notes again, this may be impractical. In a plasma of a density closer to that used in short pulse systems, or our UT^3 system, the driving pulse would need to be around 14 fs, which is not a pulse duration that is very common, specifically for high intensity systems.

The last described scenario in this study [11], is the most reasonable scenario and the scenario that motivates our CPRA system. It is important to note however, that the paper outlines this last mechanism for an 800 nm driving beam and a long, 1064 nm counter-propagating beam. Therefore, an experiment on our system would naturally have different parameters.

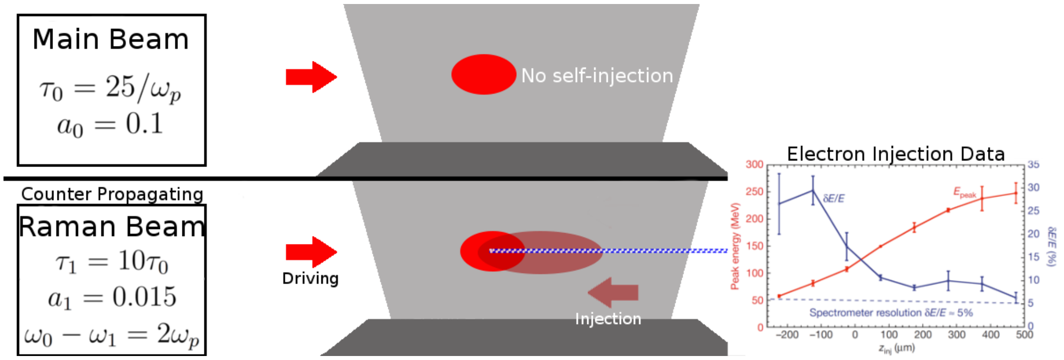

Figure 3.3: Graphical depiction of a colliding beam accelerator, showing no significant electrons when the driving beam is by itself (top), and then showing example electron data [21] when the injection beam is involved (there are various proposals for these beams, and the parameters listed are just one such example from [11]). The example data is from an experiment showing injection from a single counter-propagating beam of the same color and is only a guide.

This last scenario, also a more conventional CBA, has two beams. The driving beam is of duration $\omega_p \tau_L \sim 25$, and the colliding pulse is of a much longer duration. The beams are detuned by twice the plasma frequency, and the colliding pulse is significantly less intense. This scenario should lead to enhanced accelerating gradients and electrons (see Fig. 3.3).

A concluding note, which I believe is important, is that the last and most relevant experimental scenario that is purported to lead to enhanced acceleration was done with a driving TiSapph beam (800 nm) and a counter-propagating Nd:YAG beam that is not doubled (1064 nm). These numbers are obviously different than what our CPRA system is capable of, and it may be that the same phenomenon is not possible with our system. Because the study is done with a much longer counter-propagating pulse ($\tau_1 \sim 10\tau_0$), our Raman beam would have to be stretched significantly. Additionally, because the detuning must be $2\omega_p$, this limits the density that we would operate with to a

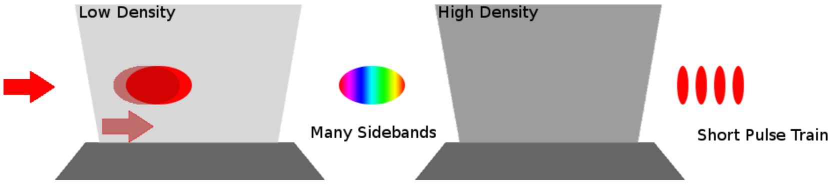

Figure 3.4: An example setup for creation of a very short duration pulse train using two stages and two beams of different color. The first gas jet is low density in order to produce many sidebands, and the second higher density jet (with high GVD) is used to compress these sidebands into a train of very short pulses.

lower value than studied. These effects combined lead me to believe that the enhancement of the accelerating gradient would be lower in our system than in the scenario described in the reference. An up to date computational study should be done to confirm this suspicion.

3.4 Laser Pulse Compression

This section is a summary of the scenario proposed in [12].

It is possible using a two-stage plasma setup, or with adequate parameters a single stage setup, to create many optical sidebands and subsequently compress them into a train a very short (few femtoseconds) pulses. This requires an input of two beams offset in frequency by the plasma frequency and of approximately the same amplitude.

In the two stage setup, the first stage would contain a low density plasma in order to create a cascade of sidebands. This cascade would then be compressed using the high group velocity dispersion (GVD) of a second stage of higher density plasma (Fig. 3.4).

The generation of the sidebands is a complex process, but can be viewed as a "complicated interplay between the GVD of radiation and the sideband coupling through th driven electron density perturbations, the nonlinearities due to the relativistic increase of the electron mass, and the forward stimulated Raman scattering (FSRS)." [12]. Luckily, the analysis in the reference takes all of these effects in to account.

Simulation parameters for the two-stage system show that for production of a total of 16 sidebands, 4.1 cm of length in the first stage at a low density of $8.75 * 10^{17} cm^{-3}$. This is a stage that would need to be created for our system. The second stage is of a density much closer to where our nozzle operates (1 mm length is needed) and therefore would not need to be added to our system. However, the single stage system operates at a higher density. This is in order to provide compression in the same stage as the creation of the sidebands. It may be that single stage method is appropriate for our current setup on the UT^3 laser system.

It is important to note however, that this computational study was not done at parameters specific to the UT^3 CPRA system. It may be that at the detuning that we are forced to have, the mechanism is significantly different. It also may be (and is more likely), that our gas jet system would need to be significantly changed in order to be successful with this experiment. Before this experiment is attempted, I suggest further computational study with parameters relevant to the UT^3 system (800 nm and 873 nm beams), and a more in depth study of the changes that would be required to the interaction chamber.

Chapter 4

Raman System Performance

This chapter will provide some characterization of the amplified and compressed Raman beam along with possible test experiments.

4.1 Ionization with Raman Beam

Using three separate methods (simple calculation, air ionization, and helium ionization) we estimate that the Raman beam intensity is on the order of $10^{17} W/cm^2$ when focused close to the optimum focused size of 10 μm FWHM in the UT^3 system.

4.1.1 Simple Calculation

The first method to calculate the intensity is a simple calculation from the measurement of the three relevant parameters: Pulse length, pulse energy, and focused beam radius. These values were measured with a background free 2nd order autocorrelator, a calibrated power meter, and a relay imaging

Method	Estimated Intensity
Simple Calculation	$2.2 * 10^{17} W/cm^2$
Air Ionization	$1.2 * 10^{17} W/cm^2$
Helium Ionization	$2.2 * 10^{17} W/cm^2$

Table 4.1: Table summarizing the estimated on-target intensity using three different methods explained in the following sections.

system imaging the focal plane on to a CCD respectively. If we take measured values for these three parameters: 200 fs, 50 mJ, and 10 μm FWHM we can calculate the intensity from the following formula [23]:

$$I = \frac{2E}{\pi \tau_p w_0^2} \tag{4.1}$$

This simple calculation results in an on-target Intensity of $2.2 * 10^{17} W/cm^2$.

4.1.2 Ionization in Air

The second method used is an experimental verification of the Intensity via the ionization of air. This estimation uses the measurement of focal spot size and subsequent Gaussian propagation, and a characterization of the produced ion channel at atmospheric density.

Because the beam is approximately Gaussian, the beam radius as a function of axial position can easily be calculated knowing the focal spot size. Although our imaged beam is rather astigmatic - 10 μm x 16 μm FWHM - this can be taken in to account when we characterize the Gaussian propagation. However, the astigmatism was not completely characterized, and is partly due to the asymmetric shape before the focusing element and separate misalignment of the focusing element. This adds to the many sources of error in the following calculations. The spatial mode was a measured parameter from a relay imaging system on to a CCD, measured at a pulse energy low enough such that ionization did not occur.

The ionization channel in air was imaged using a simple digital camera and a long exposure time. The total length of this channel was shown to be 18±1 mm. We will use the standard Gaussian optics formula [23] to find the

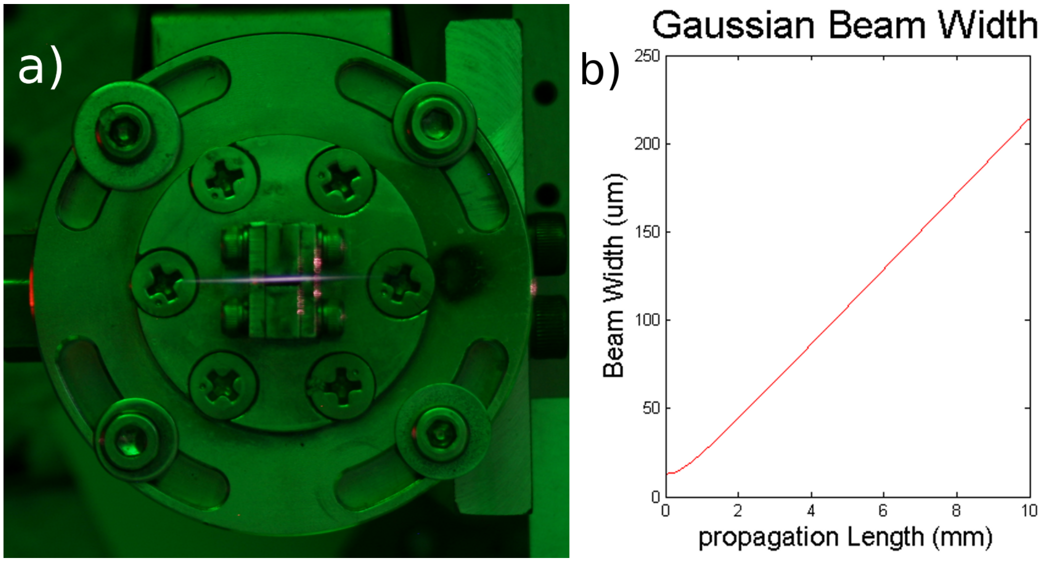

Figure 4.1: (a) Long exposure photograph of the ionization channel made by the Raman beam in air with a total length of 18±1 mm. (b) plot of (average) Gaussian beam radius as a function of position for this beam.

size of the beam at the beginning of the channel:

$$w(z) = w_0 \sqrt{1 + \left(\frac{z}{z_R}\right)^2} \tag{4.2}$$

where $z_R = \pi w_0^2/\lambda$ is the Rayleigh range of the beam. This relation applies to each axis when the beam is astigmatic.

We combine the length of the channel with the calculated beam radius at the beginning of the channel to find the relationship between the focal spot intensity and the ionization intensity for air. In this case the focal spot intensity must have been approximately 470 times the air ionization threshold, when comparing the astigmatic Gaussian beam area at the waist and after 9 mm of propagation.

At intensities below $1 * 10^{14} W/cm^2$ the ionization rates in air are low and the nitrogen in air is not fully ionized [24]. However, there is short pulse ionization data [25] that shows the ionization threshold of air with 200 fs pulses to be around $2.5*10^{14} W/cm^2$. Using this we can finally calculate the on-target, focused intensity to be approximately $1.2 * 10^{17} W/cm^2$.

Note that because this is a long exposure photograph it may be that longitudinal instability in the position of the focus artificially extended the length of the ion channel. However, it may also be the case that all of the ionization did not produce visible side-scatter, which would mean our measurement was a under-estimation of the intensity. Because these effects are not quantified and are competing with each other, no qualification of the measurement will be made. These possible systematic errors combined with the inadequately described astigmatism of the focus must lead the reader to not take this as an exact measurement, but as an estimate of the order of the beam intensity at focus.

4.1.3 Ionization in Helium

We undertook a similar procedure to again measure the intensity via ionization of a gas. In this case we focused the Raman beam through the helium gas jet under vacuum conditions. However, due to measurement difficulties the data we were able to get was not as complete (Fig. 4.2).

Instead of acquiring an image of the ion channel, we could only achieve observations at discrete points. And even so, these observations are qualitative. At different longitudinal positions of the gas jet we observed the ion channel as the whole length of the gas jet (3 mm), as roughly half of the length of the gas jet, and as barely visible. From this we can produce a similar deduction of

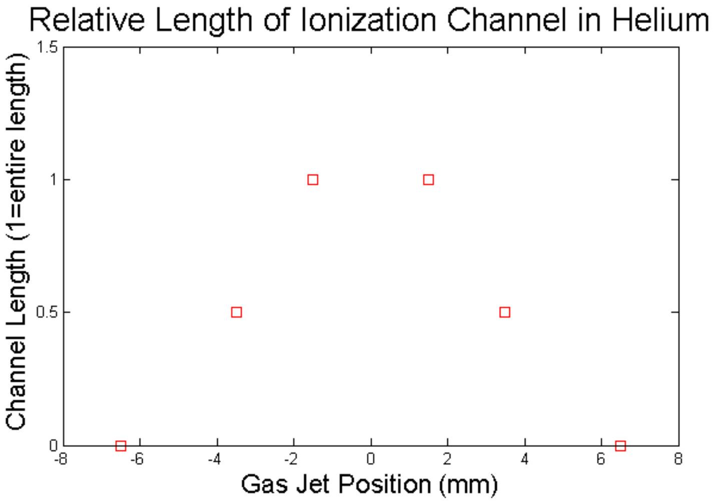

Figure 4.2: Simple diagram of what was observed in the ionization of helium by the Raman beam. At various longitudinal positions of the gas jet the ion channel length was observed to be either the full length of the jet, half of the length, or barely visible. This is represented by 1, 0.5, and 0 on the y-axis.

the region of the Gaussian beam propagation that is intense enough to ionize helium.

We calculate the "half-length" of the channel to be 5±0.5 mm, which resulted in a calculation of the focal spot intensity being roughly 145 times the ionization intensity threshold for helium (using the exact same method as in the previous section). Again using literature sources [26, 27] to justify an ionization threshold for helium at $1.5 * 10^{15} W/cm^2$, the focal spot intensity was calculated to be $2.2 * 10^{17} W/cm^2$ assuming only first ionization at the beginning of the channel.

Again in this case there are many possibilities for error in addition to the fact that our measurements are inherently rough. However, it is another data point to guide and confirm the order of magnitude of the peak beam

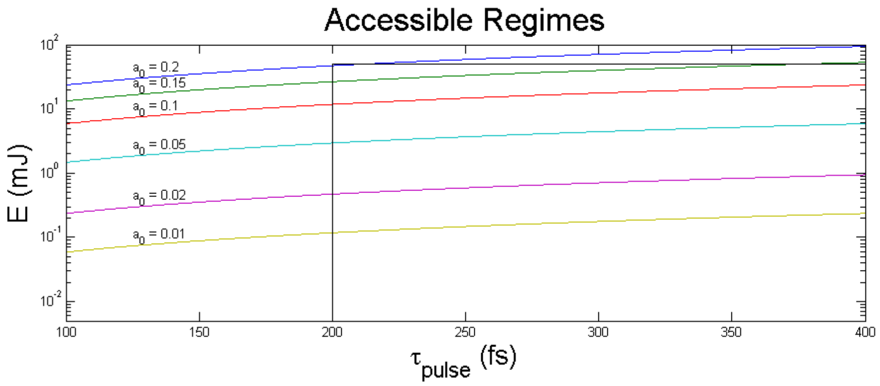

Figure 4.3: A diagram of the accessible regimes of our CPRA system resulting from the ionization measurements. Note that the maximum a_0 is essentially 0.2, and the accessible region is the lower right area constrained by the black lines. This is for a focused spot size of 10 μm FWHM.

intensity.

4.1.4 Accessible Regimes

Because we are limited by an upper-bound on-target energy of 50 mJ and a lower-bound pulse duration of 200 fs, there are only certain accessible regimes. Although usually a_0 is the quoted parameter, especially to note whether relativistic effects are important, many of the experiments possible for this system not only have desired ranges for intensities, but also may require different pulse durations. Because of this it is important to know what regimes are actually possible given one or more constraints.

Because we will almost always focus to the ideal spot size of 10 mum, our limits are energy and pulse duration. A plot of the accessible regimes (contours of constant a_0) of pulse duration and energy are shown in Fig. 4.3 with the accessible area above 200 fs in duration and below 50 mJ in energy.

4.2 Test Experiments

This section concisely outlines two examples of test experiments that the Raman beam is surely capable of, and are also possible diagnostics for time overlap (Section 5.4). It must be noted that at different points in time these have been attempted with little success. However, they are not the primary motivation for the use of the CPRA system.

4.2.1 Spectral shifts in the Raman Beam as a Probe

The wakefield produced from a high-intensity laser pulse can exist for many plasma wavelengths after the driving laser pulse. It is a structure that can be used to create nonlinear effects.

In [28] a high intensity laser pulse experiences spectral modifications due to the effects of this periodic structure caused by the laser pulse itself. This is an example of the Raman instability, and a very good example of nonlinear optics within a plasma at relativistic intensities.

In [29], a probe beam at significantly different wavelength than the driving pulse experiences spectral modifications due to the plasma wake. In this case the time delay was changed and the existence of the Raman sidebands in this probe was shown to appear and then disappear, providing a temporal characterization of the plasma wake under those driving conditions.

Although this experiment is not in any way a motivator for our own CPRA system, it does have similar qualities and may be a test experiment to show the ability to overlap our 873 nm beam with the wakefield produced by our 800 nm beam. However, we must be careful to not be near the bubble regime, because those conditions may not provide a wakefield that will properly

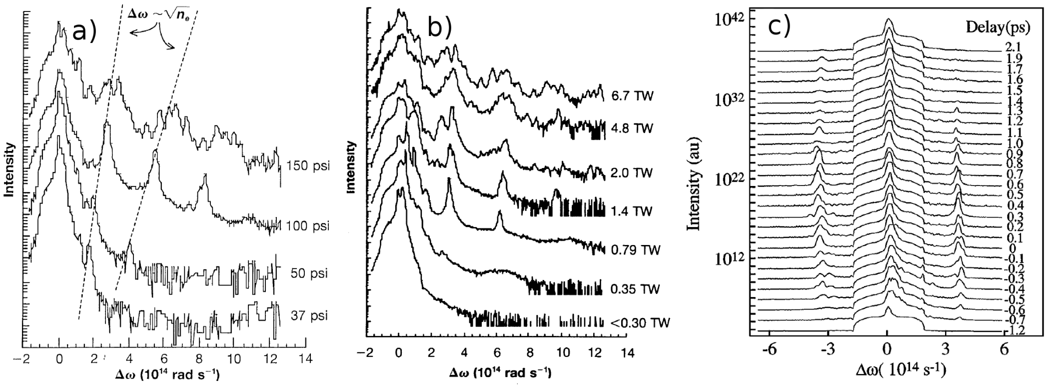

Figure 4.4: Data from previous experiments showing (a) the change in Raman sidebands with plasma density in a driving pulse, (b) the change in those sidebands at a constant density with varying driving intensity, and (c) the Raman sidebands for a weak witness beam at a different wavelength for various time delays. (a) and (b) are from [28] and (c) is from [29].

affect the probe. Therefore, both the main beam and Raman beam would be operated at intensities significantly below their maximum.

It also should be noted that, if observed, these effects could be used as a diagnostic of temporal overlap for purposes of achieving the goal (Raman seeded LWFA) experiment.

4.2.2 Seeded Relativistic Cross-Phase Modulation

Relativistic cross-phase modulation (Appendix D) has been previously observed in high-intensity laser-plasma experiments [30]. However, in this experiment the Raman satellite was not a separate produced laser beam, but rather a result of the forward Raman scattering instability. Therefore, although it was of course observed and characterized, our system has the ability to show the same phenomenon with an intense Raman satellite that has been separately produced, amplified, and focused.

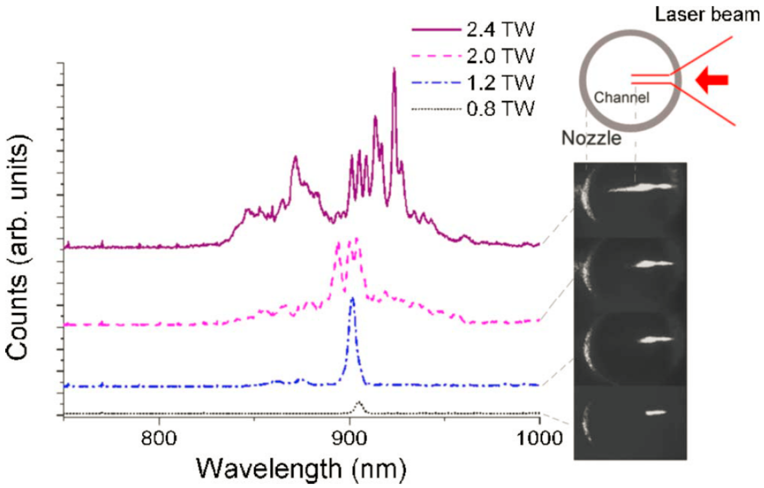

Figure 4.5: Data showing the broadening of the Raman satellite as incident driving intensity increases. This is the onset of relativistic cross-phase modulation. Taken from [30].

Again, this experiment is not a significant motivator, but is a good example of nonlinear optics in a plasma, and could be used as a final diagnostic for *exact* time overlap within the plasma.

Chapter 5

Raman Seeding Experiment

This chapter will outline our progress on the experiment geared towards seeding the forward Raman instability as outlined in Fomyts'kyi, 2005 [8]. Our goal is to both observe spectral shifts, new sidebands, or amplification of the existing Raman sideband along with production of MeV level electrons (SM-LWFA regime) when only the seed is present in addition to the driving pulse.

5.1 Experimental Description

This experiment is exactly the experiment described and motivated by [8]. There is also a detailed background in Section 3.1.

The goal is to use our 873 nm beam from the CPRA system and overlap it in all three dimensions with the more powerful 800 nm main beam produced by the main UT^3 system. This overlap, with proper pulse durations and resonant plasma density will seed the forward Raman instability and produce electrons at a significantly lower driving intensity than is normally required for the self-modulated wakefield regime.

Both the main beam and the Raman beam will be compressed to approximately 200 fs, and focused to comparable sizes onto the entrance of the supersonic gas jet. The main beam will be below the critical power for self-focusing and the Raman beam will be at a much lower energy than the main

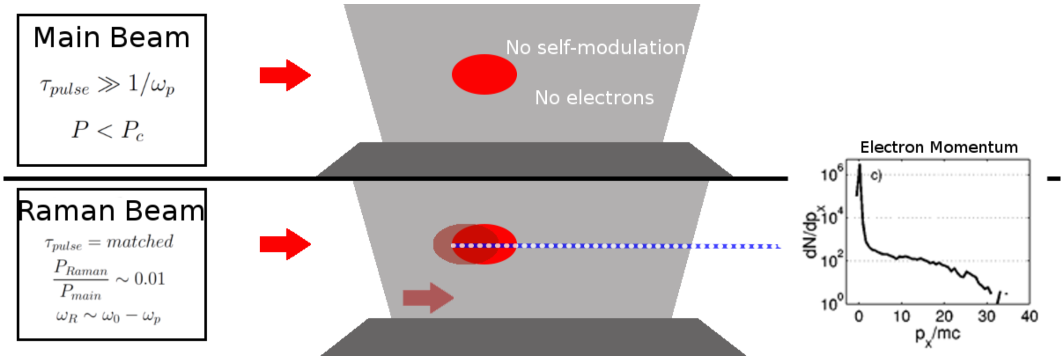

Figure 5.1: Conceptual image explaining the experimental setup and expected result from the Raman seeding experiment. The two beams will be completely overlapped in the plasma. We hope to create conditions where there are significant spectral modifications and continuous electrons up to 10s of MeV when only the two beams are overlapped.

beam. The resonant density, i.e. the plasma density that will allow for the 873 nm beam to seed the Raman instability caused by the more intense 800 nm, is equivalent to approximately 10 PSI backing pressure on our gas jet with the focus 500 μm above the gas jet exit (Section 5.3).

The initial parameters for the main beam should be such that electrons will not be produced at any energy comparable to those produced from self-modulated wakefields. In other words, the main beam alone focused in to the plasma will not produce observable electrons. However, we hope that with the Raman beam overlapped and collinear the instability will be properly seeded and electrons will be produced.

The main beam and Raman beam will be overlapped just after compression and will have identical beam paths before entering the interaction chamber (Fig. 5.2). They will then be focused onto the gas jet entrance via a f/13 Off-Axis Parabola (OAP). They will be relay imaged onto separate CCDs

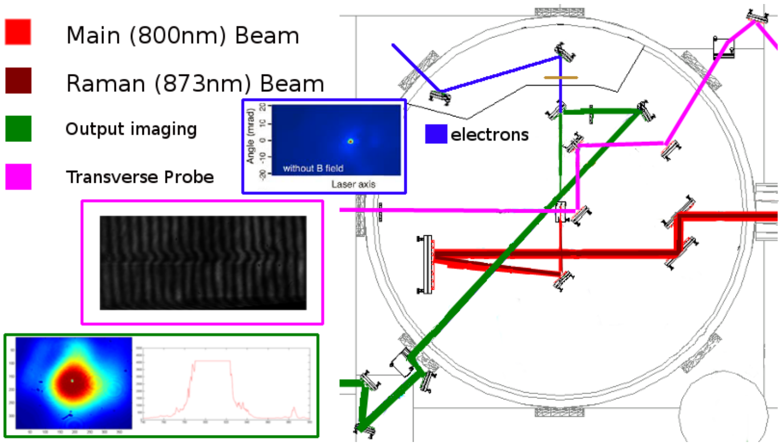

Figure 5.2: Layout of the wakefield chamber and diagnostics for the Raman seeding experiment. The output imaging is used for spatial mode characterization and output spectrum, and the transverse probe is used for interferometry. The electron beam diagnostic is used to look for a signal alone rather than to characterize the electron spectrum.

after exiting the chamber.

The first diagnostic, which will first help us find time overlap (Section 5.4) and will finally be used to see growth in the 873 nm signal, is a simple fiber spectrometer. This is located in the same line as the output imaging system. We hope that this will provide an indication of forward Raman instability seeding and successful conditions for electron acceleration.

Lastly, the electron beam diagnostic (LANEX) is the most crucial diagnostic. We hope to see a signal of electrons only when the main beam and Raman beam are overlapped. As a first test this diagnostic will not include a deflecting magnet. This is a more simple configuration, although the magnet could be included later to also measure the energy of the electrons.

Conditions
$\omega_p = 1.22 * 10^{19} cm^{-3}$
$\tau_{pulse} \gg 12$ fs
$E_{main} < 480$ mJ

Table 5.1: Table summarizing the necessary conditions to seed the forward Raman instability and produce electrons.

5.2 Necessary Conditions

There are three crucial experimental parameters that must be met, and optimized in order to achieve the regime described in [8]. These three parameters are plasma density, pulse duration, and pulse energy. This is no surprise since these factors determine the power of the lasers and the specific class of behavior that will occur in the plasma.

First, and most importantly, the plasma density must be set to be resonant with the beat frequency of the two incident laser pulses. Because the wavelengths are not tunable, this is not a changing parameter. A straightforward calculation leads to a resonant plasma density of $1.22 * 10^{19} cm^{-3}$. The next section details how this condition is achieved.

Second, the pulse durations involved must be significantly larger than the "matched" wakefield time. Specifically $\tau_{pulse} \gg 2.3548/\omega_p$ where the factor of 2.3548 comes from the conversion from RMS to FWHM, and $1/\omega_p$ is the matched condition in non-bubble regime wakefields (Appendix A). Because the plasma density had already been determined this is another straightforward calculation that results in: $\tau_{pulse} \gg 12$ fs. Because our Raman beam can only be compressed to ~200 fs, we match both beams to this duration, which provides significant overlap and satisfies the condition.

Lastly, the driving pulse energy (800 nm pulse) must be subcritical.

This is because we want the interaction to be thoroughly away from the bubble regime, or even the regime of self-focusing. This means the power of the driving pulse must be below the critical power (see Appendix C): $P_c = 16.8(\omega/\omega_p)^2$. Again, because we know the resonant plasma frequency, this calculation is simple and results in an on target strict maximum energy of $\sim$480 mJ. This is a simple target to meet and is near the threshold of our system. We will operate significantly below this energy.

5.3 Gas Jet Characterization

Although the supersonic gas jet that we operate with has been roughly characterized in order to successfully produce monoenergetic electrons [19], there did not exist a complete characterization of the density at different backing pressures. Additionally, because the optimum for producing the electrons is about $1.9 * 10^{19} cm^{-3}$ and our resonant density for Raman seeding is $1.22 * 10^{19} cm^{-3}$ we did not have a point of reference.

Using the sparse data provided to us by H.-E. Tsai, along with data for a similar nozzle existing in [31] I created a linear relationship between the backing pressure behind the solenoid (stagnation pressure) and the density at a distance of 500 μm above the exit of the nozzle.

$$n_e = 0.008272 * P - 1.3367 \tag{5.1}$$

Where P is the Pressure in PSI and n_e is the plasma density (Helium) in units of $10^{19} cm^{-3}$. It is possible that this is an overestimation of the plasma densities at pressures above 200 PSI, but the linear relationship is clear between 20 PSI and 200 PSI, which I have confirmed via the interferograms in

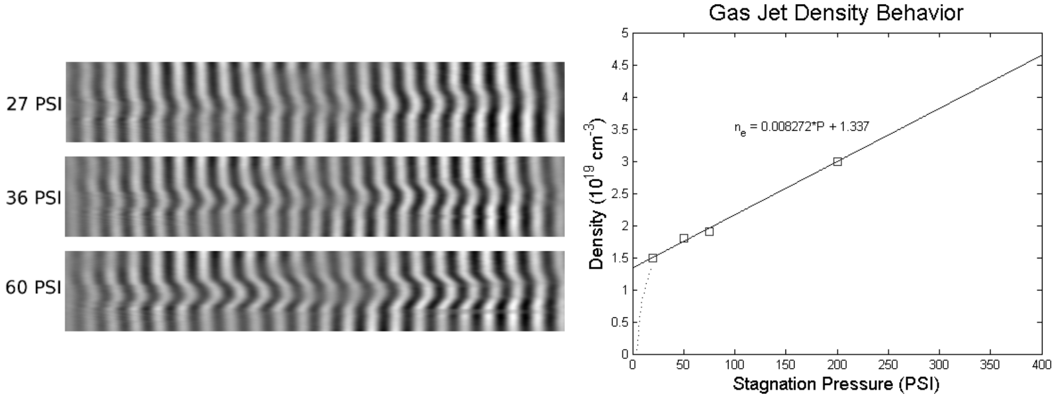

Figure 5.3: Three separate interferograms showing the plasma channel and induced phase difference on the transverse probe at three backing pressures (left). The gas jet was previously characterized at only four points by H.-E. Tsai (squares), which was simply fit to a line (right). The dotted line shows qualitative expected behavior below the measured values. The interferograms were cleaned up via 2D-FFT filtering.

Fig. 5.3. At present we do not have the data for pressures above 200 PSI.

Although this is phenomenological, the agreement is good with the data that we have, albeit not thorough. This relationship serves as a good guide and is similar to the expected behavior for a supersonic nozzle in general. However, it is clearly not accurate much below 20 PSI, where the density must drop off dramatically. Because we expect the density to drop off very quickly below 20 PSI, it is reasoned that a pressure of **17.5 PSI** should be used to achieve the desired results for the Raman seeding experiment.

5.4 Temporal Overlap

This experiment requires that both the driving pulse (the pulse that creates the wake) and the modulating pulse be mostly temporally and spatially overlapped for the phenomenon to occur. This is as expected because of the

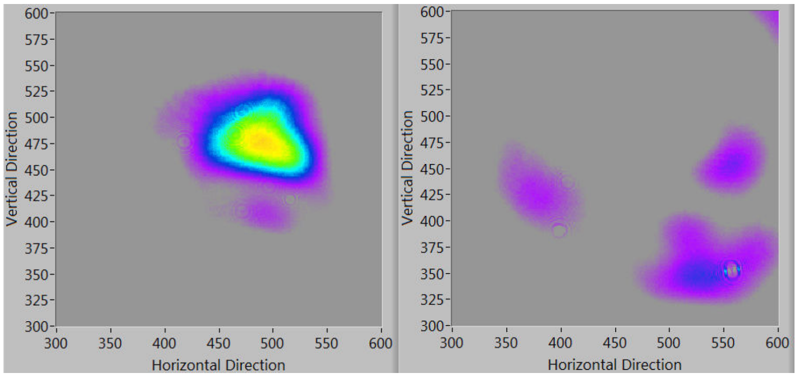

Figure 5.4: Figure showing the difference in transmitted Raman pulse when there is no main beam present (left) and when there is (right). There is a clear qualitative change in the spatial mode meaning that the main beam has arrived before and created a plasma leading to defocusing of the Raman beam. Courtesy of J.C. Sanders.

nature of the Raman instability. The modulation in electron density must beat with the incident strong field in order for the instability to grow. This happens in space, and thus requires an overlap condition in all three dimensions.

Spatial overlap transverse to the laser direction is relatively simple. The two beam are rough-aligned onto the same path after being separately compressed. Then fine alignment onto the focusing parabola and the target is done. Other fine adjustments like input collimation, etc. are also done, but the process is in general straightforward.

Temporal alignment however, which is responsible for overlap in the direction of propagation, is not so straightforward. First of all, because we are dealing with 200 fs pulses we are looking for arrival accuracy on the order of 60 μm. This presents difficulty, which is mostly rooted in the instability of the Raman beam itself.

The first method to get a rough temporal overlap is to observe defocusing of the Raman beam caused by the ionization of air by the main beam, as shown in Figure. 5.4. The Raman beam must be at an intensity that does not cause significant ionization and the main beam must be intense enough to cause significant ionization itself. Therefore, the Raman beam will only experience defocusing caused by the plasma channel when it is either partially overlapped, or behind the main beam by single picoseconds.

The diagnostic to view ionization defocusing is the relay-imaged output mode of the lower energy Raman beam. As we slowly delay the Raman beam in time the onset of defocusing signals also the beginning of overlap. However, this effect will be most significant once the Raman beam is actually behind the main beam, that it is not a good enough tool to get complete overlap of the beam themselves. Therefore ionization defocusing in air can only be a rough diagnostic of temporal overlap of the beams.

It is possible however, to again follow this procedure in vacuum using instead the helium gas jet rather than air. Because Helium has a larger ionization intensity the technique is inherently more accurate with Helium. Again, for the same reasons as before, this can only be a rough technique. Therefore, we must rely on other techniques to try to achieve the desired complete overlap of the 800 nm and 873 nm pulses.

The test experiments described in Section 4.2 are actually possible techniques for testing the overlap. These are regimes that are somewhat similar to the regime that we will use to achieve the Raman seeded LWFA, and rely on spectral diagnostics to achieve overlap. The first experiment (Section 4.2.1) does not require perfect overlap, but the second experiment (Section 4.2.2) ideally does. In this way they can provide increasing confirmation of our temporal overlap. For this reason we use the output spectrum as an other primary diagnostic for temporal overlap once the chamber is in vacuum conditions.

First we look for sidebands produced at wavelength above the 873 nm beam, signally alignment within ∼1 ps. Next we look for broadening of the 873 nm pulse itself, meaning that we are overlapped.

It must be noted that these effects are only significant at much higher plasma densities than the resonant density for Raman seeding. Because of this the time overlap diagnostics will be done at a high gas jet pressure. Once overlap is achieved the pressure will be decreased in order to seed the forward Raman instability and proceed towards the goal experiment.

5.5 Spectral Measurements

The spectrum was a diagnostic tool to observe Raman shifting in the 800 nm driving beam by itself, to attempt to confirm temporal alignment based on previous results [29, 30], and to observe the expected growth of the Raman seed after proper time overlap was achieved. Unfortunately, we have to this point only observed the Raman scattering instability in the driving pulse alone, no two-color effects, and no effects that suggest seeding of RFS.

Our first observation was modulations above 1100nm that are not a Raman shift, but rather from some other mechanism. Our second, and more relevant observation was a first Stokes sideband at very high gas jet pressures. Unfortunately, due to the small spectral distance between the Raman beam and the very broad main beam (800 nm with modulations almost to 850 nm, and the 873 nm Raman beam), the likely weakness of Raman shifts at lower pressures than those observed, and the lack of ability to achieve a relativistic driving beam at these pulse durations, no other spectral modifications or enhancements were observed.

The first spectral modifications observed were the single, double, or triple peaks stretching from above 1100 nm to the end of the range of our spectrometer (1238 nm) as seen in Figure 5.5. These may be half harmonics from the very end of the ionization based modulations below 800 nm that are very significant. These ionization modulations (Fig. 5.6) are not necessarily consistent, but can extend all the way to 600 nm, which would result in the half harmonic just being visible in the upper wavelength range of our spectrometer. Subharmonic generation has been observed and predicted in plasmas previously [32, 33], but mostly from solid targets or other non-uniform plasmas. They are often some type of coupling between ion acoustic waves and electron density waves.

This explanation of a half harmonic is far-fetched. The ionization modulations do not have a long propagation in order to seed the process and the physics necessary is not present in any significant way. It may be, however, that these observed infrared peaks are just an artifact of the spectrometer. For example, a third order diffraction of second harmonic light produced by the driving beam. Because we do not have a convincing description, no conclusion will be made on their origin except that they are not an RFS signal.

The consistency of the location of theses peaks regardless of gas pressure acts as confirmation that this is not a Raman shift, in addition to these peaks not generally being consistent with the expected location of Stokes sidebands (See Table 5.7). Therefore these peaks, although ubiquitously present, are not considered in our analysis.

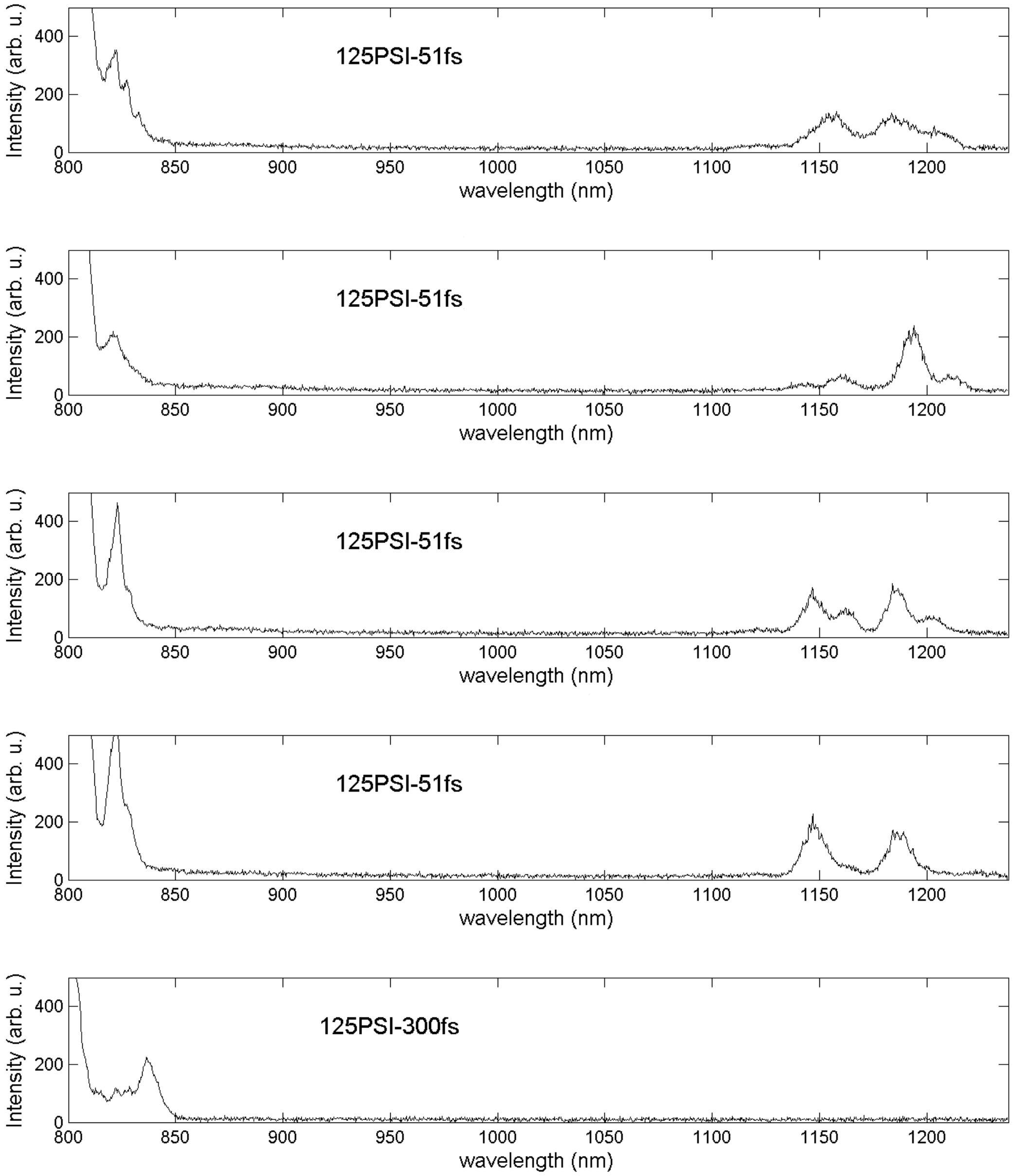

Figure 5.5: (top four) Examples of modulations seen with a 51 fs, 330 mJ main beam incident on the gas jet at 125 PSI. Note that the modulations disappear once the pulse is stretched to 300 fs (bottom) with all other settings the same. All modulations below 800 nm are left out of the plots. The peak just below 850 nm is present in the main beam without any gas interaction.

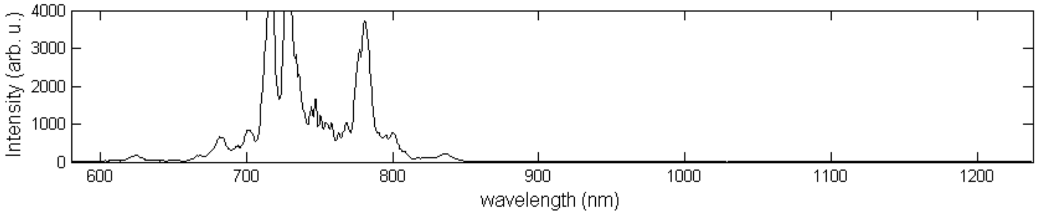

Figure 5.6: Example of modulations below 800 nm caused by ionization and self-phase modulation thereafter. This is for a 325 mJ main beam at 300 fs duration incident on the front edge of the gas jet at 125 PSI.

5.5.1 Unseeded Raman Forward Scattering

The second and more relevant spectral modification observed was the first Stokes Raman sideband from the driving laser pulse incident on the gas jet, without the co-propagating Raman beam. We observed, mainly at high gas pressures, a first Stokes sideband near where it is expected for a driving pulse centered at 800 nm and the calculated plasma densities from our rough linear model (See Table 5.7).

The comparison must be made between Figures 5.5 and 5.7. They both are with the same alignment of the laser beam, gas jet position, and laser pulse energy. The differences are pulse duration and gas jet pressure. It is very clear that at 125 PSI there is no Stokes sideband and that at 300 PSI there is a clear sideband. It is also the case that the infrared signal discussed previously exists at both gas pressures at similar central wavelength.

A final note that is important to this analysis is the comparison between our rough plasma density model and the observed location of the Stokes sideband. Comparing the location of the Stokes sideband to the expected values we observe, the peaks are consistently at lower central wavelength. This would correspond to an over-estimation of the plasma density. As discussed

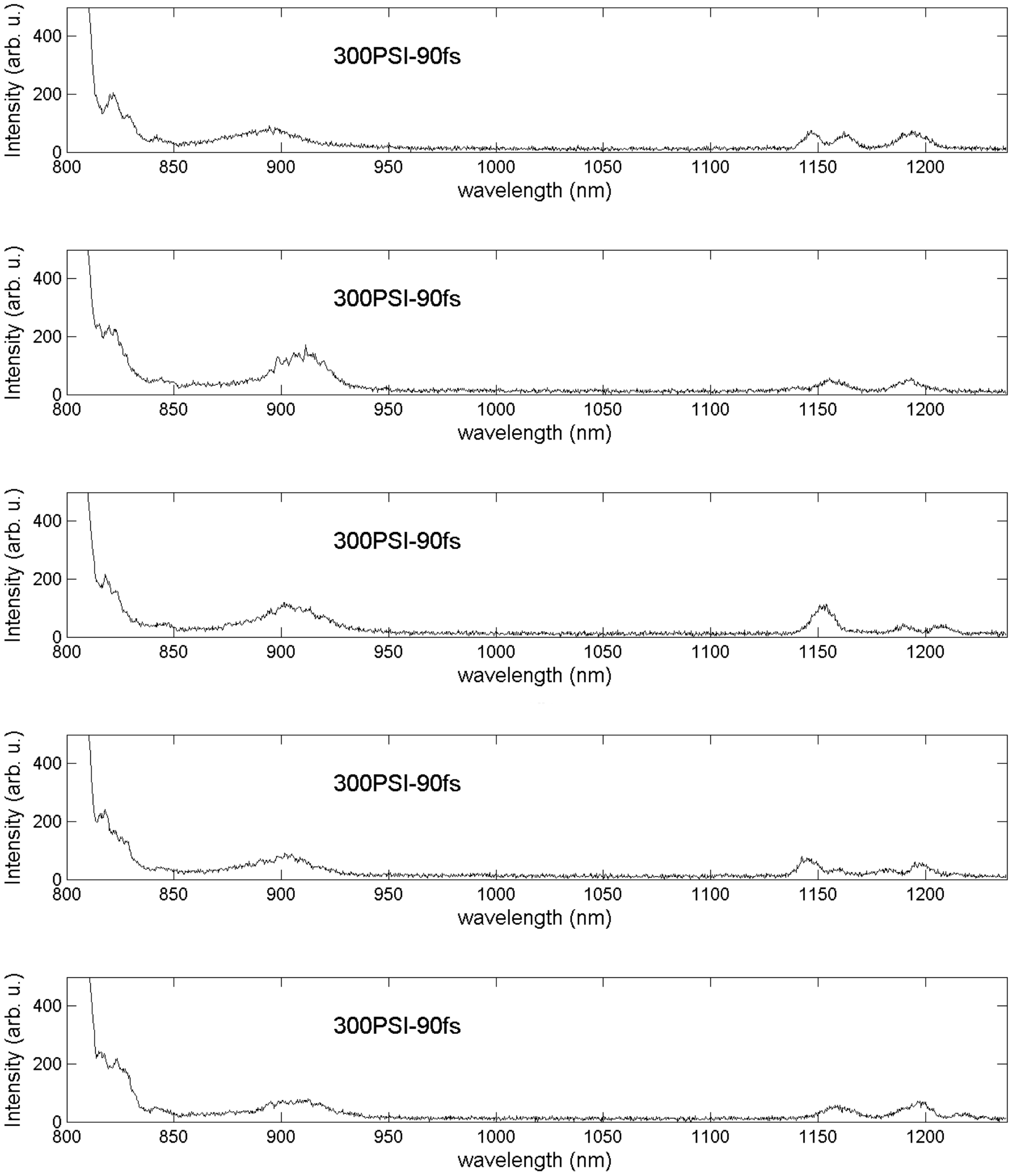

Figure 5.7: Five examples of modulations seen with a 90 fs, 330 mJ main beam incident on the gas jet at 300 PSI. Note the peak slightly above 900 nm, which was not present in the shots at 125 PSI, and the sustained peaks between 1100-1200 nm. All ionization related modulations and otherwise below 800 nm are left out of the plots.

before this is likely the case due to our sparse data for plasma density. However, because there are extremely significant modification to the main beam spectra, and they are almost exclusively below 800 nm, it may be that the Stokes is not exclusively pumped by 800 nm. This would also result in a lower central wavelength for the Stokes sideband. The author is not able to separate these two potential effects. Therefore, no qualification will be made.

Unfortunately, none of the spectral modifications that would have either served as corroborating diagnostics of time overlap, novel tests of our two-color system, or signs of seeding of RFS were observed. We can only hope to barely observe RXPM at the intensities that we were operating at (due to the stretched pulse), and the weakness of the Raman shifts in the main pulse do not provide a good prospect for observing them in the Raman pulse. However, we did very thoroughly determine overlap and most disappointingly did not observe any enhancement of RFS, at or below the critical power. The next section details our observation of SM-LWFA electrons, but no evidence of enhancement and no electron signal below critical power.

5.6 Electron Measurements

Electron measurements in this experiment come from a LANEX phosphor screen that is 30 cm after the gas jet. Output imaging optics within the interaction chamber are moved out of the way by motors, and the electrons are meant to impinge on the phosphor screen. This screen produces light that is then imaged on to a CCD for data collection.

For our preliminary experiments there was no deflecting magnet, although we do have a large magnetic field magnet, which deflects the electrons in order to measure the energy spectrum of said electrons. We are looking first for just a signal of electrons, which is why we are not concerned with the energy spectrum.

Our first step was an attempt to view electrons in the same way that has been previously done in the bubble regime, with the main pulse by itself at full power and full compression [19]. We were provided a procedure of steps to follow in order to *optimize* the electron signal, but of course we only desired to see *any signal* to confirm that the diagnostic worked.

Unfortunately, due to below optimum performance of the laser system we were not able to operate at or above $2 * 10^{18} W/cm^2$ (or a_0 =1). We were only operating at $5 * 10^{17} W/cm^2$ (or a_0 =0.5). Because of this we did not see any bubble regime electrons even with a thorough scan of gas jet density and z-position of the gas jet. Therefore, the next purpose of the electron beam diagnostic was to attempt to observe electrons from either the main beam by itself, or with the Raman beam overlapped. These electrons would now be characteristic of the self-modulated wakefield regime.

5.6.1 SM-LWFA Electrons

The UT^3 laser system is not optimized to produce electrons in the self-modulated laser-wakefield acceleration (SM-LWFA) regime. Lasers that have generally operated in this regime are much longer pulse, Nd:Glass lasers or otherwise that also have significantly higher pulse energy. However, we have observed electrons in the SM-LWFA regime from our pulse stretched significantly, and at very high gas pressures (plasma densities).

As was outlined in detail in Section 5.5, we observed Raman forward scattering (RFS) from the main beam by itself. However, we only observed this signal at densities far above the resonant density for our seeding experiment.

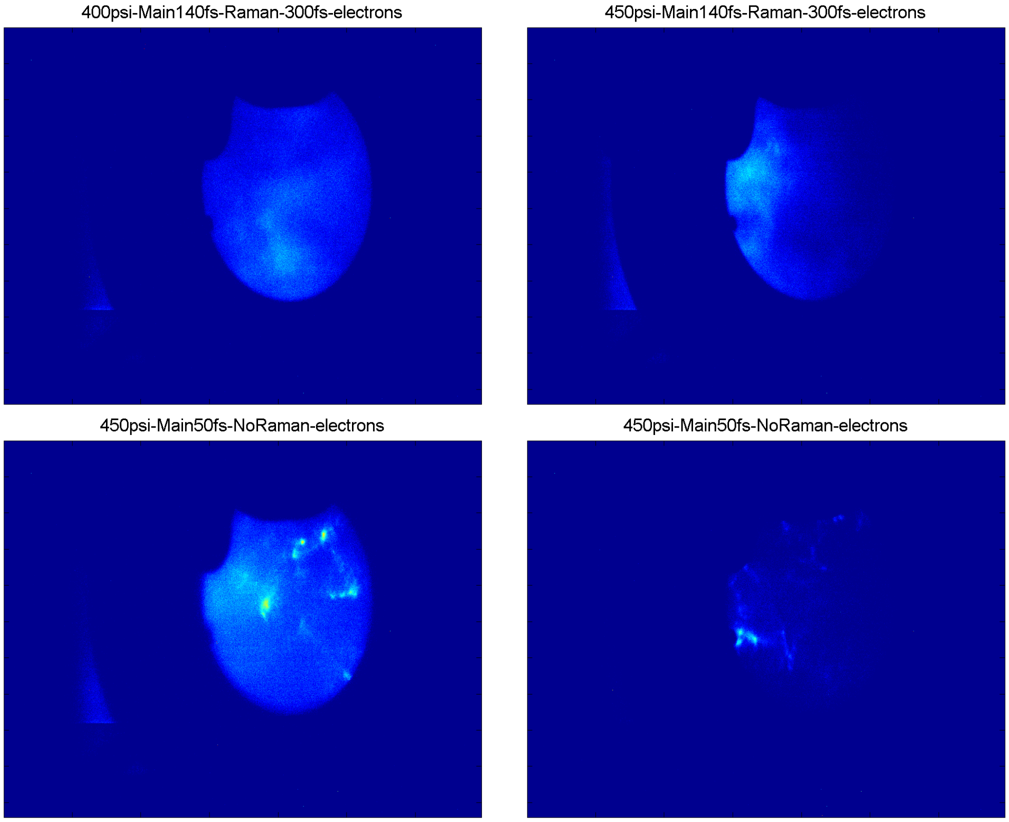

400psi-Main140fs-Raman-300fs-electrons

450psi-Main140fs-Raman-300fs-electrons

450psi-Main50fs-NoRaman-electrons

450psi-Main50fs-NoRaman-electrons

Figure 5.8: The four best examples of observed electrons from both the stretched and fully compressed main pulse. Note that the top two both have the beam overlapped, but the electrons signals are not obviously enhanced. We observed electrons even at a 50 fs duration (bottom two) due to the very high density, but never observed electrons at a density even close to the much lower resonant density. We also did not observe electrons at driving powers below the critical power with the Raman beam overlapped (the goal experiment) or otherwise.

Because of this we did not observe any spectral sign that would suggest seeding of RFS. Additionally, in any of the regimes where we first observed the RFS signal, we did not see any electron signal.

However, we did observe an electron signal at densities even greater than where we first observed RFS and therefore even further away from our resonant density. These electrons are ostensibly from the SM-LWFA regime, and are very divergent and low in total charge. Figure 5.8 shows the four best examples of these electrons.

5.7 Concluding Remarks

To summarize the results of our most recent experiments, we have not been successful in seeding FRS and therefore not observed any of the effects predicted in [8]. However, we have observed FRS in the main UT^3 pulse stretched to durations above 90 fs, and we have also observed (most likely very low energy) electrons produced from the SM-LWFA conditions created in that regime. Despite the fact that our plasma density calculations may be an over-estimate above 200 PSI, the intuition from scaling laws (Table 5.7) confirms why we did not have the ability to seed FRS, why we saw FRS signals when we did, and provides a guide for moving ahead.

First and most importantly, the FRS peaks we saw were only of significant amplitude above noise at very high gas jet pressures and therefore high plasma densities. Because of this the central wavelength of the FRS signals observed was always above 900 nm, albeit not especially consistent besides that. This means that our designed seed at 873 nm is essentially useless. Unless we were able to seed at a lower density and cause the previously undetectable signal to grow, we do not have hope to seed with our 873 nm beam. We at-

P (PSI)	$n_e (10^{19} cm^{-3})$	$\omega_p (10^{14} Hz)$	λ_{1S} (nm)	λ_{2S} (nm)	$P_c (TW)$	$2/\omega_p$ (fs)	τ_c (fs)
25	1.54	2.22	883	986	1.89	9	172
50	1.75	2.37	889	1001	1.67	8	195
75	1.96	2.50	895	1016	1.67	8	218
100	2.16	2.63	901	1030	1.49	8	241
125	2.37	2.75	906	1044	1.35	7	264
150	2.58	2.87	911	1058	1.23	7	287
175	2.78	2.98	916	1071	1.13	7	310
200	2.99	3.09	921	1085	1.05	6	333
225	3.20	3.20	926	1098	0.98	6	356
250	3.40	3.30	930	1111	0.86	6	379
275	3.61	3.40	935	1124	0.81	6	402
300	3.82	3.49	939	1137	0.76	6	425
325	4.03	3.59	944	1150	0.72	6	448
350	4.23	3.68	948	1163	0.69	5	471
375	4.44	3.77	952	1176	0.66	5	494
400	4.65	3.85	956	1189	0.63	5	518
425	4.85	3.94	961	1202	0.60	5	541
450	5.06	4.02	965	1215	0.58	5	564

Table 5.2: Table summarizing the conditions available to us at various gas densities, where λ_{1S} is the wavelength of the first Stokes Raman (λ_{2S} is the second) sideband with an 800 nm pump and τ_c is the duration that the pulse must be below (with 325 mJ on target) to be over the critical power. This assumes the linear relationship between gas pressure and plasma density at pressures above 200 PSI, which is likely to be an over-estimate.

tempted this and did not observe any seeded growth. Therefore, it does not seem to be feasible to seed with our CPRA beam. Additionally, the 873 nm is so close spectrally to the main beam that any spectral effects would be very difficult to observe to begin with.

One may ask, is it inevitable that the Raman signal is only observable at such high densities? The answer unfortunately is yes. In this regime we are operating at much longer pulse durations than is normal. Because our beam can only be slightly above relativistic ($a_0 = 1$) conditions at the most ideal operation, our power and intensity are significantly lowered when the pulse is stretched, which compounds the fact that ideal operation is just that *ideal*, and not normal. If we understand the fact that in order to see an FRS signal we must have a pulse duration significantly larger than k_p of the plasma ($\tau_L \gg 2/\omega_p \propto n_e^{-1/2}$), and that we must be significantly over critical ($P_l > P_c \propto n_e^{-1}$), then as the density increases we improve both our chances of seeing

FRS (i.e. the window of pulse durations where it is even possible increases) and we increase the expected growth over the distance of the plasma [34].

This confirms what we observed, that as we increase the plasma density, we have a stronger FRS signal. In the specific instance of our experiment and our laser parameters this means that only at pressures above 200 PSI and more assuredly 300 PSI can we hope to see a "good" FRS signal.

Therefore the natural extension of this discussion is that we should firmly operate at high pressures and change the type of beam that we use to seed the process. J.C. Sanders has been investigating alternate options for creating a Raman sideband closer to where we have seen our FRS signal (∼925 nm) from the compressed main pulse. Additionally we have been assessing the practicality of instead using the second Stokes sideband of the $BaNO_3$ crystals in the CPRA system, which is also in the range of wavelengths that we have seen so far. These feasibility studies have not yet been concluded.

Chapter 6

Conclusion

The basic conclusions of our work on the Raman Seeding experiments is that it does not seem to be feasible with our CPRA beam as it is currently operated. We observed a first stokes RFS sideband from the main driving beam, but only at high enough plasma densities such that our 873 nm beam is not useful.

However, it may be possible to use the second stokes sideband from the $BaNO_3$ crystals in the CPRA system, amplify that in the 6-pass TiSapph amplifier, and compress that with our set of compressor gratings. Although that would most certainly result in lower gain through the system and potentially worse pulse compression, it may be that it is sufficient. Another alternate method would be to forgo the CPRA system as a whole and use the compressed main beam to produce a Raman sideband in the newly found wavelength range (915 nm - 940 nm) with a Raman active gas or liquid. The feasibility of these solutions is not yet determined.

The motivating theoretical predictions (Chapter 3) are almost exclusively based on computational work and also have explored parameters that are not the same as our system. The discovery that the Raman seeding experiment is not likely to be feasible with our current CPRA operation is significant and suggests that the same may be true for the Colliding Beam Accelerator, Suppression of Relativistic Self-Focusing, and Laser compression experiments.

It would be instructive and helpful to guide the current and future line of research into these experiments if a computational study was done for these phenomenon with parameters directly relevant to our system (with a proper chirp in the driving pulse if it is above a 35 fs pulse duration).

The motivations for these experiments are important and significant. Although we have not yet been successful on producing any result, if proper modifications are done there is still the possibility of a result. However, a more thorough and relevant computational study should be done to confirm our expectations on the UT^3 laser system.

Appendices

Appendix A

Laser Wakefield Acceleration

Please note that this appendix borrows heavily from Eric Esarey's 2009 review of the topic [15]. Figures are borrowed from that same resource, along with many of the equations. Supplementary resources are also noted.

This appendix will provide a concise outline of laser wakefield acceleration and some recent results at University of Texas at Austin.

A.1 The Mechanism in General

Laser wakefield acceleration is a process by which an intense laser beam can be focused into a gas target, create a plasma, and then a plasma wake, which can accelerate electrons. The phenomenon was famously describe in [1] before the lasers necessary were actually possible. Since the development of very high power lasers [2], these experiments have become possible and the field is very active. The UT^3 laser system is highly invested in wakefield acceleration and many of the experiments in the lab deal with related physics.

The crucial mechanism, without going in to great detail, is that the presence of the laser ionizes the gas creating a plasma, and then causes plasma waves to form. In the linear regime, $a_0 \ll 1$ the response is the very familiar "Langmuir waves". Or, simple electron density waves oscillating at the plasma frequency, ω_p. However, a crucial result of intense lasers being tightly focused and intense, the ponderomotive force (see appendix in [35]):

$$\mathbf{F}_p = -m_e c^2 \nabla (a^2/2) \tag{A.1}$$

a force that essentially acts on the gradient of laser intensity, causes nonlinear plasma waves or ”wakes” to occur. These result in a large axial electric field. It is this axial field, in all regimes, that is responsible for the acceleration of particles. Particle acceleration along with radiation as a result of those particles are the largest motivators of work in laser-based acceleration.

A.2 Nonlinear Regime

The nonlinear regime is the regime where the laser intensity becomes large enough for the nonlinear terms in the fluid equations to be significant. Another way to phrase it is that a perturbation based analysis is no longer correct. Rather than an in-depth analysis, a short graphical explanation can communicate important details.

Fig. A.1 shows two important results from analysis of the nonlinear wakefield regime. First, that as laser intensity (measured by a_0) increases the density response becomes significantly more sharp. This can be seen by the difference between the dotted curves trailing the laser pulse (located at $k_p\zeta = 0$) in graphs (a) and (b). Additionally, the magnitude of the accelerating electric field is larger for a more intense laser pulse.

The second significant result is that the accelerating electric field (E_z) changes depending on the length of the laser pulse. It is shown to have an optimum when the length of the pulse, L_{rms} is matched to the plasma wavelength.

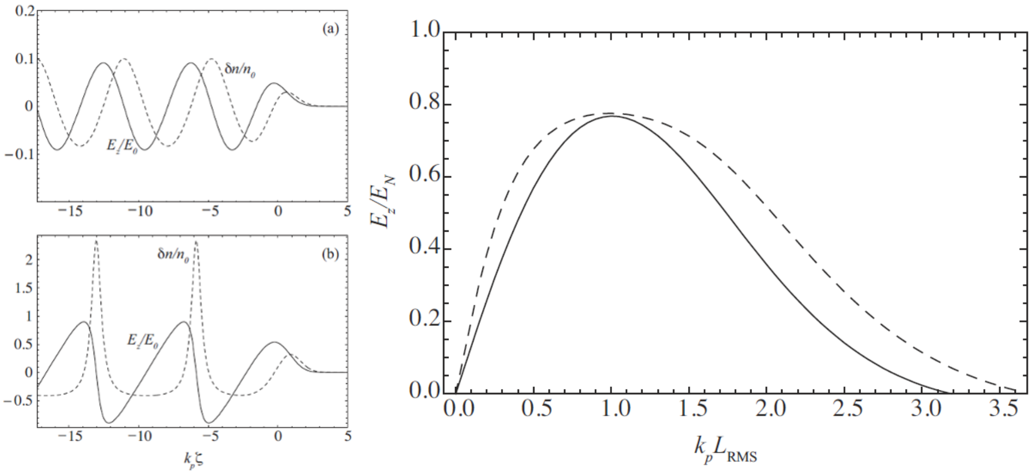

Figure A.1: Left: ”Time-averaged density variation $\delta n/n_0$ (dashed curve) and axial electric field E_z/E_0 (solid curve) in an LWFA driven by a Gaussian laser pulse (pulse is moving to the right, centered at $k_p\zeta = 0$ with rms intensity length $L_{rms} = k_p^{-1}$) for (a) $a_0 = 0.5$ and (b) $a_0 = 2.0$.” Right: ”Amplitude of axial electric field E_z [normalized to the maximum amplitude of a flat-top pulse $E_N = (a_0^2/2)/(1+a_0^2/2)^{1/2}$] plotted as a function of laser pulse length k_pL_{rms} for the LWFA examples shown in ...(the left images)... : $a_0 = 0.5$ (solid curve) and $a_0 = 2.0$ (dashed curve). The laser pulse envelope is $a = a0 \exp -\zeta^2/4L_{rms}^2$.” Taken from [15] with permission.

It is also shown that this optimum is not especially sensitive to the intensity. This second result is ever-present in current experimental infrastructure.

A.3 Self-Modulated Regime

The self-modulated regime is a somewhat intermediate regime bridging the nonlinear and bubble scenarios. However, there are a few very key differences that set the self-modulated regime apart from the other two.

First of all, the driving pulse is actually much longer than the matched condition, so that $\tau_L \gg 1/\omega_p$. The reason that this is the case is so that Raman forward scattering (RFS, Appendix B.3) can modulate the beam, which creates a beatwave driven ponderomotive force. These phenomena can cause enhanced acceleration in the wake of the driving pulse. Low energy electrons were seen at first [36], but with an appropriately over-critical and relativistic beam (25 TW, duration 800 fs, $n_e = 1.5 * 10^{19} cm^{-3}$), wave breaking was observed in electrons accelerated up to 44 MeV [22], and electrons have been injected via Raman backscatter [37].

The resulting continuous electron energy spectrum has been well understood in the years since. However, the bubble regime is required to see monoenergetic electrons of significantly higher energies.

A.4 Bubble Regime

The bubble regime, or blow-out regime as it is sometimes called, is a result of the laser intensity being so large that rather than a sharp nonlinear wake, a cavitation of electrons occurs. This cavitation or ”bubble” produces an even larger charge separation and accelerating field. This regime is very similar to what is called the ”blowout” regime, but the nuanced difference will not be discussed here. The bubble regime again uses shorter, matched pulses similar to the nonlinear regime.

Fig. A.2 shows the results of particle-in-cell simulations of laser wakefield acceleration in the bubble regime. The color scale on the left denotes the electron density, and the graphs on the right are lineouts of the field. It is important to note that because of the very high nonlinearity, computer simulations are almost completely necessary to elucidate dynamics in this regime.

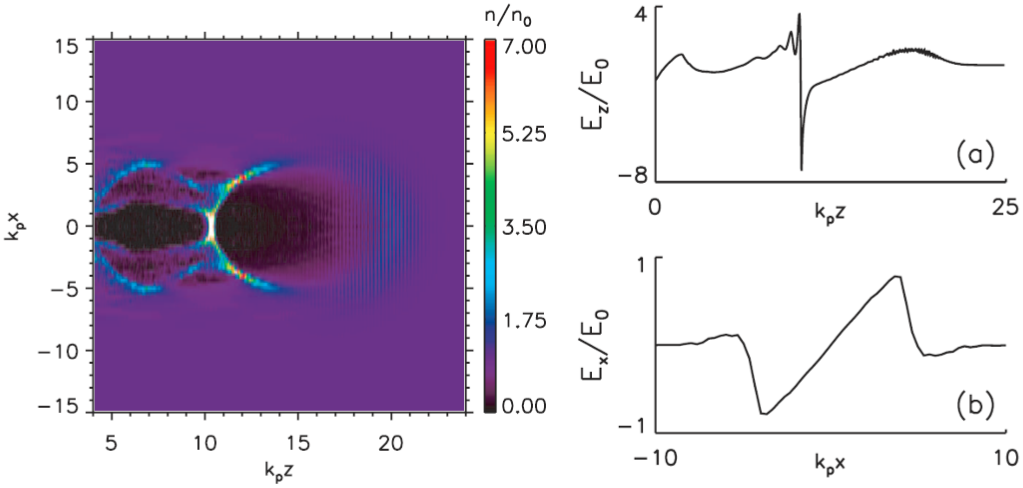

Figure A.2: Left: ”(Color) Electron density wake at $\omega_p t = 27.7$ driven by a laser pulse with an initial envelope given by $a = a_0 exp(z^2/2L^2) exp(x^2/r_0^2)$ with $a_0 = 5$, $L = 4.2\mu m$, $r_0 = 9\mu m$, and $\lambda = 0.8\mu m$. The laser is propagating to the right in a plasma of density $n_0 = 7x10^{18} cm^3$...” Right: ”Lineouts of (a) longitudinal electric field on axis (b) and transverse electric field at $k_p z = 13$ for the parameters of ...(the left image)... at $\omega_p t = 27.7$.” Taken from [15] with permission.

A.5 Limitations

Although plasma based acceleration seems to have gone over the field strength limit imposed in conventional accelerators, the method is not without its own limitations. The most serious are referred to as pump-depletion and dephasing. Depletion results from the laser itself losing energy and therefore no longer being able to drive a strong wake. Dephasing is a result of the electrons actually having a larger velocity than the group velocity of the light in the plasma. This results in the electrons moving out of the optimum accelerating position in the wake (or bubble) and no longer accelerating.

Scaling laws have been developed in two regimes for both of these important limitations [15, 38, 39].

$$L_d \simeq \frac{\lambda_p^3}{2\lambda^2} \begin{cases} 1, & \text{for } a_0^2 \ll 1. \\ (\sqrt{2}/\pi)a_0/N_p, & \text{for } a_0^2 \gg 1. \end{cases} \tag{A.2}$$

$$L_{pd} \simeq \frac{\lambda_p^3}{\lambda^2} \begin{cases} 2/a_0^2, & \text{for } a_0^2 \ll 1. \\ (\sqrt{2}/\pi)a_0, & \text{for } a_0^2 \gg 1. \end{cases} \tag{A.3}$$

Where N_p is the number of wake periods behind the drive pulse. These are commonly referred to as the dephasing length (L_d) and depletion length (L_{pd}). Note the density dependence of each ($\lambda_p \sim n_e^{-1/2}$).

In addition to inherent limitations due to the mechanism itself, acceleration depends on high coupling of the laser pulse to the plasma and an avoidance of plasma instabilities. It has been shown that both the focal spot[40] and the shape of the density profile[41] effect the success of wakefield acceleration.

A.6 Texas Petawatt Results

It is clear that in order to accelerate electrons to high energy one must have a very intense laser pulse, adequately matched to the plasma wavelength, and be able to accelerate for a long distance. Although many experiments utilize Ti:Sapph amplifier systems operating at 800 nm, these short pulses require a high density to be matched and therefore this technique has a short dephasing length.

M.C. Downer's team at the University of Texas has taken a different approach aided by the existence of the Texas Petawatt laser (1057 nm). Due to the longer pulse duration (160 fs) the laser is matched to a much lower density and therefore can accelerate for a longer length. Because of the large

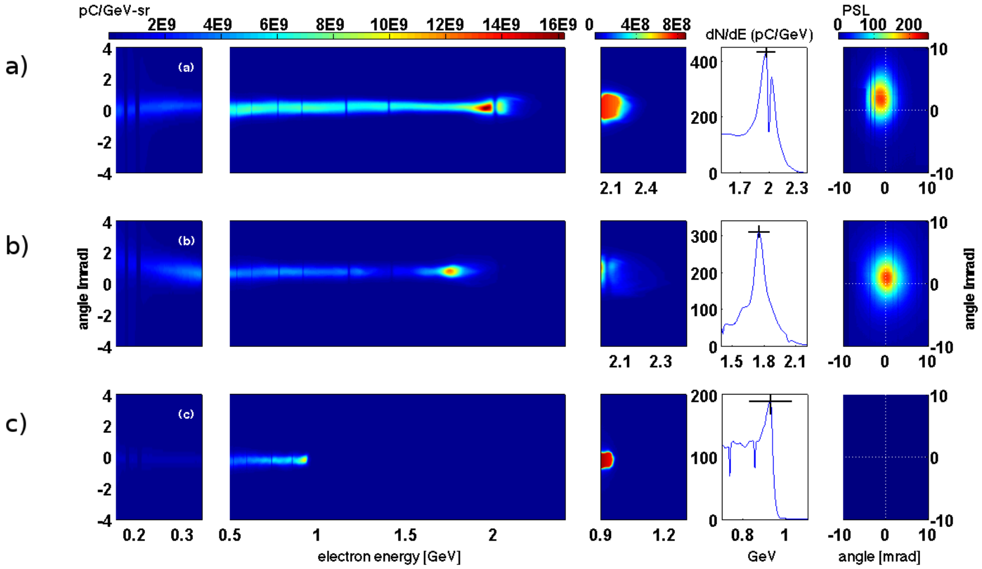

Figure A.3: Electron Energy Spectra and Betatron X-ray profiles for three Texas Petawatt LWFA shots. the left three columns are energy spectra in certain regimes, and the far right column is the profile of the Betatron X-rays. Shots (a) and (b) both have quasi-monoenergetic peaks at 2.0 GeV and 1.8 GeV respectively and the first has high energy tails up to 2.3 GeV. All shots have low energy tails. Courtesy of X. Wang and N. Fazel and similar to a figure from [3].

pulse energy, this is still a relativistic beam and can create a bubble. Use of the Petawatt laser has resulted in world record electron energies[3] of above 2 GeV (Fig. A.3). It is relevant to compare this to other GeV work in, for example, gas-filled capillaries [42].

Upcoming upgrades to the pulse contrast and improvements in the focal spot on the Texas Petawatt may result in even higher electron energies, consistent with idealized computational work [43].

Appendix B

Raman Scattering

This appendix borrows heavily from [13] and [14]. Please consult these texts for a more detailed treatment.

This section will outline the Raman scattering phenomenon as both a general nonlinear optical process, and as a laser-plasma instability.

Raman scattering [44] is often explained as a resonance of two laser wavelengths to a molecular vibration frequency within a medium. Raman scattering was first experimentally observed in 1962 [45], and studied in detail in the years following.

B.1 In General

Light propagation through any dielectric medium is a function of the development of a polarization density and associated radiation. Linear processes depend on the "polarizability" of the medium, which can be viewed in the Lorentz model as related to the effective spring constant and radiative damping of the relevant electrons in the atoms. Nonlinear processes depend on a similar relationship, but now the "hyper-polarizability" is a tensor, which relates two components of the incident field to the induced polarization (at some multiple of the incident frequency).

In the Lorentz model the polarizability is calculated through a damped and driven harmonic oscillator analysis of the electrons displacement from equilibrium. However, it is assumed that this is just a value that relates Electric Field strength to Polarization density. Raman scattering must be viewed as a result of the linear polarizability depending on the same displacement from equilibrium [13], and therefore changing in time.

$$\alpha(t) = \alpha_0 + \left(\frac{\partial \alpha}{\partial x}\right)_0 x(t) \tag{B.1}$$

The behavior of $\alpha(t)$ is not know *a priori*, but if we believe that it will be periodic then this variation in polarizability can also be viewed as an induced periodic variation in the refractive index.

Now the effect of this relationship must be included in the force analysis, which was once a simple damped and driven harmonic oscillator. If we look at the amount of work needed to produce this new term in the polarizability, then the following can be confirmed.

$$\mathbf{F}_{Raman} = \frac{\epsilon_0}{2}\left(\frac{\partial \alpha}{\partial x}\right)_0 \left\langle E^2(z,t)\right\rangle \tag{B.2}$$

If we guess a trial solution for the total electric field, including both the incident laser light and what we believe to be produced "Stokes" light ($\omega_L - \omega_S = \omega_v$, ω_v is the frequency of the molecular vibrations), then we proceed to calculate the following expression for the amplitude of the molecular vibration:

$$x(\Omega) = \frac{(\epsilon/m)\left(\frac{\partial \alpha}{\partial x}\right)_0 A_L A_S^*}{\omega_v^2 - \Omega^2 - 2i\Omega\gamma} \tag{B.3}$$

and the following for the nonlinear polarization:

$$\begin{aligned} P^{NL}_{Raman}(z,t) = \epsilon_0 N \left(\frac{\partial \alpha}{\partial x}\right)_0 & \left[x(\Omega)e^{i(Kz-\Omega t)} + c.c\right] \\ & \times \left[A_L e^{i(k_L z - \omega_L t)} + A_S e^{i(k_S z - \omega_S t)} + c.c\right] \end{aligned} \tag{B.4}$$

This solution contains many frequency components. If we look at the solution oscillating at the Stokes frequency (via $\omega_L - \omega_L + \omega_S$), and define the susceptibility as is convention we arrive at the following:

$$P(\omega_S) = 6\epsilon_0 \chi_R(\omega_S)|A_L|^2 A_S e^{ik_S z} \tag{B.5}$$

$$\chi_R(\omega_S) = \frac{\epsilon_0 (N/6m)(\partial\alpha/\partial x)_0^2}{\omega_v^2 - (\omega_L - \omega_S)^2 + 2i(\omega_L - \omega_S)\gamma} \tag{B.6}$$

If analysis is done on the propagation of the Stokes wave, then it is shown to be a pure gain process with a growth rate in the z direction (which is normally written as an absorption rate, which is negative) of:

$$\alpha_S = -3i\frac{\omega_S}{n_S c}\chi_R(\omega_S)|A_L|^2 \tag{B.7}$$

So, the Stokes beam grows throughout the length of the medium.

It must be noted that a Quantum Mechanical description of Raman scattering has been similarly well developed, and is exactly equivalent [46].

B.2 In a Plasma

The Raman scattering process in a plasma is similar conceptually, but very different to compute. Essentially the incident laser light produces a density fluctuation, which produces scattered light of small amplitude. This scattered light then interferes with the initial laser light, which produces more density rippling via the ponderomotive force. This feedback loop causes the scattered light to grow.

The growth rate experienced in Raman scattering in a plasma is as follows [14, 47]:

$$\gamma = \frac{kv_{os}}{4}\left[\frac{\omega_{pe}^2}{\omega_{ek}(\omega_0 - \omega_{ek})}\right]^{1/2} \tag{B.8}$$

where ω_{pe} is the electron plasma frequency and $\omega_{ek} = (\omega_{pe}^2 + 3k^2v_e^2)^{1/2}$ is the "Bohm-Gross" frequency, which includes the thermal velocity of the electrons, v_e. The value of k depends on the exact phase matching condition, but ω_0 is the known frequency of the laser, and v_{os} is the quiver velocity of an electron in an electric field. Notice that the growth rate is larger in the backward direction, which is the same as derived for dielectric media long ago [48].

Raman scattering is therefore also observed in a plasma, but with a different growth rate and different phase-matching conditions (i.e. different frequencies for the Stokes wave). However, this analysis is only for plane waves and does not involve spatial or temporal effects that are significant for short pulses.

B.3 RFS of Short Pulses

Although the previous sections provide a good intuition for Raman scattering as a general phenomenon and specifically in a plasma, the mechanism that is important for the self-modulated regime of laser-wakefield acceleration is very different. With pulses that are significantly shorter than a Rayleigh length, what is called spatio-temporal growth becomes very important in understanding the quantitative nature of Raman scattering [34]. Because forward scattering is what is relevant to SM-LWFA, this is what will be discussed.

The work of Mori et. Al, 1994 [34] uses the 1D quasistatic approximation (time derivatives are kept in Maxwell's equations, but dropped in the fluid equations) to derive a simple growth rate of the plasma response, along with an in depth exact solution. If the plasma response is referred to as ϕ, then the quasistatic evolution of that response is:

$$\phi_s = \phi_0 H(\psi) H(\tau) I_0(2\gamma_{nl}\sqrt{\tau\psi}) \tag{B.9}$$

and the exact solution is:

$$\begin{aligned}\phi_s &= \phi_0 H(\psi) \\ &\times \left[\left[H(\tau) - H(\tau-\psi)\right] Cosh(\gamma_0 \tau) + H(\tau-\psi) \sum_n \left(\frac{\psi}{\tau-\psi}\right)^n I_{2n}(2\gamma_0\sqrt{(\tau-\psi)\psi}) \right]\end{aligned} \tag{B.10}$$

where ψ is the (normalized) position from the front of the pulse and $\gamma_0 = a_0/\sqrt{8}k$ is the growth rate of the response (k is also normalized to ω_p/c). H() is the Heaviside step function and $I_n()$ is the modified Bessel function of order n.

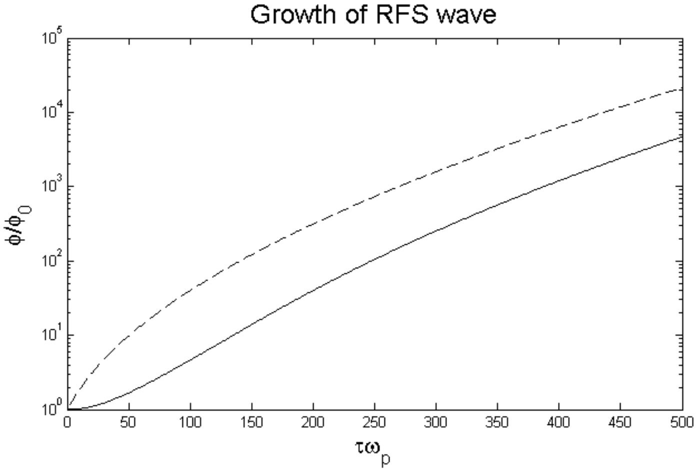

Figure B.1: Theoretical growth of RFS with parameters explored in our experiment. The dashed line is the quasi-static approximation and the solid line is the exact solution.

The literature shows two examples of this evolution. First a 5 J, 1 μm, 0.8 ps pulse representing a Livermore laser at the time, and second an I=2.2*$10^{17} W/cm^2$, 250 nm, 114 fs representation of a possible x-ray laser. Both of these cases are compared to the various approximations.

For the purpose of illustration, the parameters for our main beam stretched to 192 fs can be used to show what the evolution of RFS would be. Parameters being, 800 nm, 325 mJ, 192 fs, 15 μm spot size FWHM, and $n_e = 4 * 10^{19} cm^{-3}$. These correspond to a_0=0.41, $\omega_0/\omega_p = 6.55 = k$, and we will set ψ=150.

The results are fairly similar to the 1 μm example in the literature Because the growth is above 10^3, this provides a theoretical motivation for why we did see RFS in the UT^3 laser system with only the driving beam. Fomyts'kyi [8] provides growth rates for the seeded process, which are part of the motivation for the experiment in Chapter 5

Appendix C

Self-Focusing

This appendix follows very closely the treatment in [13] Sections 7.1 and 13.7. Please consult that reference in addition to [49] and [50] for a more detailed treatment.

In this appendix a simple model for self-focusing will be shown along with a calculation when the self-focusing occurs in a plasma with an intense incident field.

C.1 In General

Self-focusing of laser light is, as one would expect, classified as a "self-action" effect. These types of effects are a result of the presence of the laser field itself modifying the surrounding material or substance, which results in some type of modification of that same incident field.

Self-focusing in a bulk material (not a plasma yet) results in general from an Intensity dependent refractive index of a material, or $n_2 I$.

$$n = n_0 + n_2 I \tag{C.1}$$

In a way similar to that of an actual lens, the material with the field now incident upon it causes a change in the phase fronts resulting in focusing.

This can be quantified by equating the effective distance traveled by a wave at the edge of the finite incident beam, a distance w_0 from the axis with no field, and a wave on the axis where an Intensity I is present.

$$(n_0 + n_2 I) f_{SF} = \frac{n_0 f_{SF}}{cos(\theta_{SF})} \tag{C.2}$$

$$cos(\theta_{SF}) = \frac{n_0}{n_0 + n_2 I} \tag{C.3}$$

Where f_{SF} is the focal length and θ_{SF} is the angle of convergence. If we assume that the angle of convergence is very small, i.e. a paraxial approximation, then a Taylor expansion can be done to further simplify the relation (note that this approximation is equivalent to assuming that the nonlinear refractive index is small compared to n_0).

$$\theta_{SF} = \sqrt{\frac{2n_2 I}{n_0}} \tag{C.4}$$

Remembering the geometry, especially the initial width of the beam, we can solve for the focal length.

$$f_{SF} = w_0 \sqrt{\frac{2n_2 I}{n_0}} \tag{C.5}$$

C.2 In a Plasma

The case of an intense beam in a plasma can be modeled in the same fashion. Essentially there is also an Intensity dependent refractive index in a plasma. But, instead of resulting from any essential material properties it is from the modification of the plasma frequency due to the relativistic mass increase of electrons due to their quiver motion. We must solve for this n_2.

It can be shown from work in nonlinear plasma wave theory that a simple relationship between the γ of the electrons and the incident field can be written [51].

$$\gamma = \sqrt{1 + a_0^2} \tag{C.6}$$

Where a_0 is the normalized vector potential of the incident field, $a_0 = \frac{eA}{mc}$, which is proportional to the square-root of Intensity. In order to solve for n_2 we must remember the expression for refractive index in a plasma and include the relativistic effect.

$$n = \sqrt{1 - \frac{\omega_p^2}{\gamma\omega^2}} \tag{C.7}$$

Where $\omega_p^2 = \frac{n_e e^2}{m_e \epsilon_0}$ is the familiar plasma frequency.

We now have enough information to solve the problem. If we assume that the beam is only mildly relativistic, i.e. $a_0^2 \ll 1$ and use the relation between the vector potential and Intensity, then we arrive at the expression for n_2.

$$n_2 = \frac{\omega_p^2 e^2}{2 n_0^2 \epsilon_0 m_e^2 c^3 \omega^4} \tag{C.8}$$

This is the correct expression, and represents a quantitative result for self-focusing in a plasma with a mildly relativistic incident pulse. Of course this is a somewhat crude model of a flat-top beam, and curved phase fronts are approximated as straight, but it is appropriate for this analysis.

One last comment is that there exists a critical power, P_c for when self-focusing effects exactly balance out diffraction. It can be shown that when using the values for n_2 just calculated that:

$$P_c = C(\frac{\omega}{\omega_p})^2 \quad GW \tag{C.9}$$

This constant C was shown to be 6.7 in [13], but 16.8 in [50]. This is the laser power over which self-focusing is a significant effect.

Appendix D

Cross-Phase Modulation

This Appendix will outline the phenomenon of cross-phase modulation, which is an important effect in two-beam, two-color laser-plasma interaction experiments.

Self-phase modulation is a pulse propagation phenomenon that results from a medium having an intensity dependent refractive index, $n_2 I$, and a variation of Intensity with time (effectively any short pulse). Because of the time dependence of the intensity and the intensity dependence of the refractive index, different parts of the pulse experience difference nonlinear phase retardations, Φ_{NL}. If the maximum difference in phase retardation is large enough, then self-phase modulation can result in broadening of the pulse. The criteria for that case (with a $sech^2$ pulse shape) is as follows [13]:

$$I \geq \frac{2\pi c}{n_2 \omega_0 L} \tag{D.1}$$

Where n_2 is the intensity dependent refractive index, I is the intensity, L is the length of propagation in the nonlinear medium, and ω_0 is the incident center frequency. This is the intensity above which self-phase modulation results in observable spectral broadening.

Cross-phase modulation is a related phenomenon that applies to two beam propagating together in a nonlinear medium. In this scheme one beam provides the intensity to modify the refractive index and a second beam experiences that modification and is broadened. The exact effect depends on the duration and shape of the driving and "witness" beams and where they overlap, but in general results in broadening.

This effect can be seen in a plasma, especially once the intensity of the driving beam is relativistic. The same n_2 calculated in Appendix C will then be dependent on time and will cause broadening in the witness beam. This is seen in [30] and is an attempted test experiment for our own CPRA system.

Bibliography

[1] T. Tajima and J.M. Dawson. Laser electron accelerator. *Physical Review Letters*, 43:267–270, 1979.

[2] D. Strickland and G. Mourou. Compression of amplified chirped optical pulses. *Optics Communications*, 56:219–221, 1985.

[3] X. Wang, R. Zgadzaj, N. Fazel, Z. Li, X. Zhang, W. Henderson, Y.-Y. Chang, R. Korzekwa, H.-E. Tsai, C.-H. Pai, H. Quevedo, G. Dyer, E. Gaul, M. Martinez, A.C. Bernstein, T. Borger, M. Spinks, M. Donovan, V. Khudik, G. Shvets, T. Ditmire, and M.C. Downer. Quasi-monoenergetic laser-plasma acceleration of electrons to 2 gev. *Nature Communications*, 4, 2013.

[4] FEMTOLASERS Produktions GmbH. *Femtopower compact pro: Femtosecond Multi-pass Amplifier User's Manual*, 3.2 edition.

[5] F.B. Grigsby, P. Dong, and M.C. Downer. Chirped-pulse raman amplification for two-color, high-intensity laser experiments. *J. Opt. Soc. Am. B*, 25(3):346–350, 2008.

[6] Franklin Bhogaraju Grigsby. *Chirped Pulse Raman Amplifier.* PhD thesis, The University of Texas at Austin, 2009.

[7] J.C. Sanders. *(to be determined).* PhD thesis, The University of Texas at Austin, 2014.

[8] M. Fomytskyi, C. Chiu, M. Downer, and F. Grigsby. Controlled plasma wave generation and particle acceleration through seeding of the forward raman scattering instability. *Physics of Plasmas*, 12:023103, 2005.

[9] S.Y. Kalmykov, S.A. Yi, and G. Shvets. All-optical suppression of relativistic self-focusing of laser beams in plasmas. *Physics Review E*, 78:057401, 2008.

[10] S.Y. Kalmykov, S.A. Yi, and G. Shvets. All-optical control of nonlinear focusing of laser beams in plasma beat wave accelerator. *Plasma Phys. Control. Fusion*, 51:024011, 2009.

[11] G. Shvets, A. Pukhov, and N.J. Fisch. Excitation of accelerating plasma waves by counter-propogating laser beams. *Physics of Plasmas*, 9(5):2383–2392, 2002.

[12] S. Kalmykov and G. Shvets. Compression of laser radiation in plasmas using electromagnetic cascading. *Physical Review Letters*, 94(23):235001, 2005.

[13] Robert W. Boyd. *Nonlinear Optics*. Elsevier, third edition, 2008.

[14] William L. Kruer. *The Physics of Laser Plasma Interactions*. Westview Press, 2003.

[15] E. Esarey, C.B. Schroeder, and W.P. Leemans. Physics of laser-driven plasma-based electron accelerators. *Reviews of Modern Physics*, 81:1229–1285, 2009.

[16] Peter W. Milonni and Joseph H. Eberly. *Lasers*. John Wiley and Sons, 1988.

[17] S. Semushin and V. Malka. High density gas jet nozzle design for laser target production. *Rev. Sci. Instrum.*, 72:2691, 2001.

[18] S.W. Jolly, Z. He, C. McGuffey, W. Schumaker, K. Krushelnick, and A.G.R. Thomas. Stereolithography based method of creating custom gas density profile targets for high-intensity laser-plasma experiments. *Rev. Sci. Instrum.*, 83:073503, 2012.

[19] H.-E. Tsai, C.-H. Pai, and M.C. Downer. Global optimization of quasi-monoenergetic electron beams from laser wakefield accelerators. *AIP Conf. Proc.*, 1507:330–335, 2012.

[20] E. Esarey, R.F. Hubbard, W.P. Leemans, A. Ting, and P. Sprangle. Electron injection into plasma wake fields by colliding laser pulses. *Phsical Review Letters*, 79(14):2682–2685, 1997.

[21] J. Faure, C. Rechatin, A. Norlin, A. Lifschitz, Y. Glinec, and V. Malka. Controlled injection and acceleration of electrons in plasma wakefields by colliding laser pulses. *Nature*, 444:737–739, 2006.

[22] A. Modena, Z. Najmudin, A.E. Dangor, C.E. Clayton, K.A. Marsh, C. Joshi, V. Malka, C.B. Darrow, C. Danson, D. Neely, and F.N. Walsh. Electron acceleration from the breaking of relativistic plasma waves. *Nature*, 377:606–608, 1995.

[23] Anthony E. Siegman. *Lasers.* University Science Books, 1986.

[24] A. Kumar, D. Dahiya, and A.K. Sharma. Laser prepulse induced plasma channel formation in air and relativistic self focusing of an intense short pulse. *Physics of Plasmas, volume =.*

[25] W. Xiao-Lei, Z. Nan, Z. You-Bo, L. Zhi-Lei, Z. Hong-Chen, and Z. Xiao-Nong. Determination of air ionization threshold with femtosecond laser pulses. *Acta Physica Sinica*, 57, 2008.

[26] S. Augst, D. Strickland, D.D. Meyerhofer, S.L. Chin, and J.H. Eberly. Tunneling ionization of noble gases in a high-intensity laser field. *Physical Review Letters*, 63:2212–2215, 1989.

[27] S.-I. Masuda and E. Miura. Effect of femtosecond prepulse with threshold intensity for optical field ionization on electron acceleration and propagation of intense laser pulse in plasma. *Japanese Journal of Applied Physics*, 49:096401, 2010.

[28] D. Umstadter, S.-Y. Chen, A. Maksimchuk, G. Mourou, and R. Wagner. Nonlinear optics in relativistic plasmas and laser wake field acceleration of electrons. *Science*, 273:472–475, 1996.

[29] S.P. LeBlanc, M.C. Downer, R. Wagner, S.-Y. Chen, A. Maksimchuk, G. Mourou, and D. Umstadter. Temporal characterization of a self-modulated laser wakeeld. *Physical Review Letters*, 77:5381–5384, 1996.

[30] S. Chen, M. Rever, P. Zhang, W. Theobald, and D. Umstadter. Observation of relativstic cross-phase modulation in high-intensity laser-plasma interactions. *Physical Review E*, 74:046406, 2006.

[31] T. Hosokai, K. Kinoshita, T. Watanabe, K. Yoshii, T. Ueda, A. Zhidokov, and M. Uesaka. Supersonic gas jet target for generation of relativistic electrons with 12tw-50fs laser pulse. *Proceedings of EPAC, Paris, France*, pages 981–983, 2002.

[32] J.L. Bobin, M. Decroisette, and Y. Vitel. Harmonic generation and parametric excitation of waves in a laser-created plasma. *Physical Review Letters*, 30:594–597, 1973.

[33] O.M. Gradov and L. Stenlo. Nonlinear subharmoic generation in nonuniform plasmas. *Plasma Physics*, 22:727–732, 1980.

[34] W.B. Mori, C.D. Decker, D.E. Hinkel, and T. Katsouleas. Raman forward scattering of short-pulse high-intensity lasers. *Physical Review Letter*, 72(10):1482–1485, 1994.

[35] Alexander George Roy Thomas. *Studies of Laser Propagation and Mono-Energetic Electron Beam Injection in Laser-Wakefield Accelerators*. PhD thesis, Imperial College - London, 2006.

[36] K. Nakajima, D. Fisher, T. Kawakubo, H. Nakanishi, A. Ogata, Y. Kato, Y. Kitagawa, R. Kodama, K. Mima, H. Shiraga, K. Suzuki, K. Yamakawa, T. Zhang, Y. Sakawa, T. Shoji, Y. Nishida, N. Yugami, M. Downer, and T. Tajima. Observation of ultrahigh gradient electron acceleration by a self-modulated intense short laser pulse. *Physical Review Letter*, 74(22):4428–4431, 1995.

[37] C.I. Moore, A. Ting, K. Krushelnick, E. Esarey, R.F. Hubbard, B. Hafizi, H.R. Burris, C. Manka, and P. Sprangle. Electron trapping in self-modulated laser wakefields by raman backscatter. *Physical Review Letters*, 79(20):3909–3912, 1997.

[38] B.A. Shadwick E. Esarey, C.B. Schroeder, and W.P. Leemans. Nonlinear pump depletion and electron dephasing in laser wakefield accelerators. *AIP Conf. Proc.*, 737:578, 2004.

[39] B.A. Shadwick, C.B. Schroeder, and E. Esarey. Nonlinear laser energy depletion in laser-plasma accelerators. *Physics of Plasmas*, 16:056704, 2009.

[40] G. Genoud, M. S. Bloom, J. Vieira, M. Burza, Z. Najmudin, A. Persson, L.O. Silva, K. Svensson, C.-G. Wahlstrm1, and S.P.D. Mangles. Increasing energy coupling into plasma waves by tailoring the laser radial focal spot distribution in a laser wakefield accelerator. *Phys. Plasmas*, 20:064501, 2013.

[41] J. Vieira, S.F. Martins, F. Fiuza, C.K. Huang, W.B. Mori, S.P.D. Mangles, S. Kneip, S. Nagel, Z. Najmudin, and L.O. Silva. Influence of realistic parameters on state-of-the-art laser wakefield accelerator experiments. *Plasma Phys. Control. Fusion*, 54:055010, 2012.

[42] W.P. Leemans, B. Nagler, A.J. Gonsalves, Cs. Toth, K. Nakamura, C.G.R. Geddes, E. Esarey, C.B. Schroeder, and S.M. Hooker. Gev electron beams from a centimetre-scale accelerator. *Nature Physics*, 2:696–699, 2006.

[43] S.Y. Kalmykov, S.A. Reed, S.A. Yi, A. Beck, A.F. Lifschitz, X. Davoine, E. Lefebvre, V. Khudik, G. Shvets, P. Dong, X. Wang, D. Du, S. Bedacht, Y. Zhao, W. Henderson, A. Bernstein, G. Dyer, M. Martinez, E. Gaul, T. Ditmire, and M.C. Downer. Laser wakefield electron acceleration on texas petawatt facility: Towards multi-gev electron energy in a single self-guided stage. *High Energy Density Physics*, 6:200–206, 2010.

[44] C.V. Raman and K.S. Krishnan. A new type of secondary radiation. *Nature*, 121:501–502, 1928.

[45] G. Eckhardt, R.W. Hellworth, F.J. McClung, S.E. Schwarz, D. Weiner, and E.J. Woodbury. Stimulated raman scattering from organic liquids. *Physical Review Letters*, 9:455–457, 1962.

[46] N. Bloembergen and Y.R. Shen. Quantum-theoretical comparison of nonlinear susceptibilities in parametric media, lasers, and raman lasers. *Physical Review*, 133:A37–A49, 1964.

[47] D.W. Forslund, J.M. Kindel, and E.L. Lindman. Theory of stimulated scattering processes in laser-irradiated plasmas. *Physics of Fluids*, 18(8):1002–1016, 1975.

[48] N. Bloembergen and Y.R. Shen. Coupling between vibrations and light waves in raman laser media. *Physical Review Letters*, 12:504–507, 1964.

[49] C.E. Max, J. Arons, and A.B. Langdon. Self-modulation and self-focusing of electromagnetic waves in plasmas. *Physical Review Letters*, 33(4):209–212, 1974.

[50] G-Z. Sun, E. Ott, Y.C. Lee, and P. Guzdar. Self-focusing of short intense pulses in plasmas. *Physics of Fluids*, 30(2):526–532, 1986.

[51] P. Sprangle, E. Esarey, and A. Ting. Nonlinear interactions of intense laser pulses in plasmas. *Physical Review A*, 41(8):4463–4469, 1990.

Vita

Spencer Jolly was born in Evansville, IN in 1989 and soon afterwards followed his parents to the northern suburbs of Philadelphia where he spent the rest of his youth. After attending Pennsbury High School and graduating near the top of his class in 2007, he enrolled in the University of Michigan in Ann Arbor. Originally a gear-head interested in working on internal combustion engines, he widened his reach and became a physics major in his junior year at Michigan. There he took up work with high-intensity lasers and did work with Alec Thomas. He then went on to the University of Texas to work with Mike Downer. Despite enjoying his time in Texas, and enjoying the science, life had other plans. After achieving a Master's degree at UT, he will go on to do research for the Extreme Light Infrastructure in Europe, and work towards a Ph.D. in Hamburg, Germany.

Permanent address: 6 Oak Ave
Yardley, PA 19067

This thesis was typeset with LaTeX[†] by the author.

[†] LaTeX is a document preparation system developed by Leslie Lamport as a special version of Donald Knuth's TeX Program.